International Journal of Hydrogen Energy 104 (2025) 567–583

Contents lists available at ScienceDirect

International Journal of Hydrogen Energy

journal homepage: www.elsevier.com/locate/he

Thermodynamical and electrochemical model of a PEM electrolyzer plant in the megawatt range with a literature analysis of the fitting parameters

Malte Pfennig [a,*], Barbara Schiffer [a], Tanja Clees [a,b]

[a] Hochschule Bonn-Rhein-Sieg, University of Applied Sciences, Department of Engineering and Communication, Institute for Technology, Resource and Energy-efficient Engineering (TREE), Grantham-Allee 20, 53757, Sankt Augustin, Germany

[b] Fraunhofer Institute for Algorithms and Scientific Computing SCAI, Schloss Birlinghoven, 53757, Sankt Augustin, Germany

ARTICLE INFO

Keywords:
PEM
Electrolyzer
Hydrogen
Thermal energy
Modeling

ABSTRACT

In the coming years, the European Union plans to establish Proton Exchange Membrane (PEM) electrolyzers, each with a 100 MW capacity. However, the selection of their locations has not been systematically optimized to leverage potential benefits, such as utilizing waste heat from large facilities for district heating. Presently, there are hardly any corresponding system models in the literature dynamically simulating a PEM electrolyzer of this size. This paper introduces a first model approach for such systems, drawing on parameters from existing literature. It addresses the inconsistency found in the literature regarding the use of the exchange current density, which varies by a factor of 10^9. A novel optimization process is developed by using an auxiliary parameter to fit the exchange current density with a newfound condition between the anode and cathode side. The outcome is a comprehensive model of a PEM electrolyzer plant, exemplarily adapted to the Siemens Silyzer 300.

1. Introduction

The European Commission aims to achieve an installation capacity of at least 40 GW of electrolysis capacity by 2030 with new targets aiming for an ambitious 120 GW [1]. Europe's first largest Proton Exchange Membrane (PEM) water electrolyzer with 10 MW was built in the Wesseling Chemical Park near Cologne, Germany. The hydrogen produced is utilized directly on-site at the chemical park [2]. Furthermore, RWE plans to install an electrolyzer capacity of 100 MW in Lingen, Germany, and begin operation in 2024. The site is to be scaled up to a total electrolysis capacity of 2 GW by 2030 [3,4].

While there is significant discussion on the scale of capacity to be developed, the choice of location is rarely optimized with regard to its value for the local infrastructure. An approach for cost optimization is discussed in [5]. For instance, waste heat from larger plants could be used for district heating [6]. A local supply of hydrogen and waste heat could increase local security and safety of energy supply [7]. Despite this, the literature offers few system models suitable for simulating PEM electrolysis plants of such magnitude. Moreover, the parameters employed in existing models are largely arbitrary and lack a standardized basis.

A PEM electrolyzer cell comprises an anode, a cathode, and a membrane between them. Using electrical power, water is split into hydrogen and oxygen. For functional stack design, each cell includes a bipolar plate, a current collector, and a membrane electrode assembly (MEA). The bipolar plate is responsible for directing water and gases into and out of the cell. The current collector ensures even distribution of water across the MEA — the place of the chemical reaction — and facilitates the transport of the resulting gases to the bipolar plate. To support the efficient movement of water and gas, the current collector is designed to be porous. Grigoriev et al. [8] delve into the overall porosity and pore size distribution of current collectors. Moreover, the chemical reaction engenders severe environmental conditions for the materials involved. Carmo et al. [9] provide an overview of an electrolyzer, detailing its components and the materials commonly utilized.

Olivier et al. [10] provide a comprehensive overview of suitable models for different model accuracies. For this purpose, they analyzed several papers and categorized an electrolyzer model into five submodels that model different aspects. The electrochemical submodel converts electricity into chemical energy, such as hydrogen and oxygen. This model is the core of every electrolysis model. Olivier et al. further categorize the electrochemical submodel into static and dynamic approaches. In most cases, the static approach is used because the electrochemical reaction responds quickly at 50 ms, rendering dynamic effects negligible in most cases. However, the dynamic model would take these into account. The curve from the static electrochemical

* Corresponding author.
E-mail addresses: malte.pfennig@h-brs.de (M. Pfennig), barbara.schiffer@h-brs.de (B. Schiffer), tanja.clees@h-brs.de (T. Clees).

https://doi.org/10.1016/j.ijhydene.2024.04.335
Received 29 November 2023; Received in revised form 19 April 2024; Accepted 28 April 2024
Available online 7 May 2024

Nomenclature

Acronyms

BoP	Balance of Plant
CAD	Computer-Aided Design
CTC	Charge Transfer Coefficient
ECD	Exchange Current Density
MEA	Membrane Electrode Assembly
MEgy	Multiphysical Energy System Simulator
ODE	Ordinary Differential Equation
PDE	Partial Differential Equation
PEM	Proton Exchange Membrane
PID	Proportional Integral Derivative

Symbols

A	Area (m^2)
A_o	Outer Stack Area
A_{me}	Active Area of the MEA (cm^2)
a	Activity
C_p	Heat Capacity (J/K)
c_p	Specific Heat Capacity (J/(kg K))
E	Inner Energy (J)
e	Error
G	Gibbs Energy (J/mol)
H	Enthalpy (J/mol)
h	Specific Enthalpy (J/kg)
h_c	Heat Transfer Coefficient (kg/m^3)
I	Current (A)
i	Current Density (A/cm^2)
i_0	Exchange Current Density (A/cm^2)
K	Amplification Factor
M	Molar Mass (g/mol)
$\dot{m}$	Mass Flow (kg/s)
n	Number of Free Electrons
$\dot{n}$	Molar Flow (mol/s)
n_{cell}	Number of Cells per Stack
P	Power (W)
p	Pressure (Pa)
$\dot{Q}$	Heat Flow (J/s)
q	Reaction Quotient
R	Resistance (Ω)
S	Entropy (J/(mol K))
T	Temperature (K)
t	Time
U	Voltage (V)
U_{rev}	Reversible Voltage (V)
U_{ocv}	Open Circuit Voltage (V)
U_{act}	Activation Voltage (V)
U_{ohm}	Ohmic Voltage (V)
U_{dif}	Diffusion Voltage (V)
U_{tn}	Thermoneutral Voltage (V)
V	Volume (m^3)
v_{aux}	Auxiliary Value for the Optimization
$\dot{W}_{el}$	Electrical Work (W)
w	Work (J/mol)

Subscripts

H_2O	Water
H_2	Hydrogen
O_2	Oxygen
an	Anode
atm	Atmosphere
bp	Bipolar Plate
cat	Cathode
cc	Current Collector
el	Electrical
er	Error
F	Faraday
f	Formation
fp	Fitting Point
i	Variation of solid parts
id	Ideal
in	Input
j	Variation of gas substances
m	Molar Value
me	Membrane
opt	Optimal
out	Output
P	Products
$PT1$	1. Order Delay
R	Reactants
r	Reaction
re	Real
ref	Reference
S	Stack
th	Thermal
V	Voltage

Superscripts

0	Standard Condition

Greek

ν	Stoichiometric Factor
α	Charge Transfer Coefficient
δ	Thickness (mm)
η	Efficiency
λ	Water Content
Φ	$h_c \cdot A_o$ (W/K)
ρ	Density (kg/m^3)
σ	Conductivity (S/cm)
τ	Time Constant

Physics Constants

F	Faraday Constant (96 485.3415 C/mol)
R	Universal Gas Constant (8.314 462 J/(K mol))

submodel is usually represented in a U-I diagram and referred to as a polarization curve. The polarization curve depends on the temperature calculated by the thermal submodel. The thermal submodel is solved by either an ordinary differential equation (ODE) or a partial differential equation (PDE). When applying an ODE, the lumped thermal capacity model is used, and a uniform temperature is assumed for the stack.

Given that the electrochemical submodel is a fundamental element of electrolysis modeling, numerous variations of these submodels can be found in the literature. However, only one cell or a stack of up to a few watts is usually considered. Most electrochemical submodels use the Nernst equation, the activation overpotential, ohmic overpotential, and the diffusion overpotential. Nevertheless, the equations for

these voltages vary slightly, as Olivier et al. [10] show. However, the parameters for the equations are not discussed in their work.

Among the most important parameters are the reaction quotient, the charge transfer coefficient (CTC), and the exchange current density (ECD). The CTC and ECD parameters are used to fit the electrochemical submodel to experimental data. The CTC (α_{an}, α_{cat}) and ECD ($i_{0,an}$, $i_{0,an}$) for the anode and cathode side result in four parameters that can be fitted. However, an additional constraint is that the CTC should satisfy this condition: $\alpha_{an} + \alpha_{cat} = 1$. Nonetheless, based on Carmo et al. [9] often $\alpha_{an} = 2$ and $\alpha_{an} = 0.5$ are used. So, the specified bounds are often not met. Abdin et al. [11] argue that the reason these specified bounds are not met is due to a faulty analysis model. In their work, they describe the influence of different parameters on the polarization curve and fit their model to experimental data. Biaku et al. [12] perform a semiempirical study of the temperature dependence of the anode CTC value. Therefore, the cathode CTC value is set to 0.5, and the anode CTC value is fitted based on an experimental polarization curve, resulting in a temperature dependence of the anode CTC value.

The ECD is mainly used as a parameter to fit the electrochemical submodel to the polarization curve. In the literature, a specific range for the values is often used. Based on Carmo et al. [9], the ECD for the anode side ranges from 10^{-12} to 10^{-3}, and for the cathode side, it ranges from 10^{-3} to 10^{-1}. Within these ranges, the ECD values are occasionally selected arbitrarily for the purpose of fitting, similar to the approach taken by Biaku et al. Dale et al.'s approach was to fit the ECD values for the anode and cathode side to adjust the polarization curve to match the experimental data. Therefore, they use a nonlinear regression algorithm. The parameters for their optimization problem are the anode ECD, cathode ECD, and membrane conductivity. Biaku et al. [12] further optimized by making the ECD values for the anode and cathode sides dependent on temperature. Similarly, Marangio et al. [13] developed a model for a high-pressure electrolyzer, optimizing several parameters, including the ECD for both the anode and cathode sides.

However, there is no consensus in the literature regarding the appropriate range of values for the ECD. For the case of fuel cell models, Alizadeh et al. [14] conducted a parameter analysis based on different papers. Their findings indicate that the parameters do not have any physical relation to an actual fuel cell and vary in a significant range. An analogous investigation into the parameters of the electrolyzer models could not be found.

Furthermore, García-Valverde et al. [15] used three different optimization functions and compare the root mean square of deviation from the different optimization processes. However, their model primarily focuses on the ECD value for the anode side, arguing that its impact on the cathode side is minimal. This paper demonstrates that the varied functions used by García-Valverde et al. are unnecessary. Khajuria et al. [16] estimate all eight of their model parameters with a modified honey badger algorithm. In this work, a method is proposed for reducing the number of parameters. Resulting in a reduction to 4 parameters in the case of Khajuria et al.

Several studies reduce the number of parameters by using another equation for the activation overvoltage. Keller et al. [17] developed a feed-forward control loop to improve the temperature management for a highly dynamic electrolyzer. In their electrochemical submodel, they reduced the four parameters (α_{an}, α_{cat}, $i_{0,an}$, and $i_{0,an}$) to two (α, i_0) by citing [18]. The reduction yields two artificial new parameters. The relationship to the original parameters is lost.

In addition, other models used the values for the CTC and ECD based on values reported in prior research. These values have been applied to a specific catalyst material at a specific temperature. For example, Chandesris et al. [19] focused on modeling the degradation of a PEM electrolyzer.

Additionally, alternative methods exist for modeling the cell voltage of an electrolysis cell. Brezak et al. [20] developed a detailed model of an electrolyzer and analyzed the different voltage effects on the polarization curve. Furthermore, there are other approaches to modeling the cell voltage of an electrolysis cell. Bernt et al. [21] analyzed ionomer content and adopted a more substantiated electrochemical approach to model an electrolysis cell. However, due to the intricate details involved in a single cell, this approach is not explored further. Khalid Ratib et al. [22] on the other hand, modeled the electrolyzer by means of a partially equivalent electrical circuit.

The polarization curve from the electrochemical submodel depends on the temperature. The temperature of the stack is calculated by the thermal submodel, which in most cases, is described by an ODE. However, only some models fully account for the thermal submodel. According to Olivier et al. [10], the thermal submodels do not differ substantially. Tiktak [23] scaled the electrolyzer stack model linearly to calculate the heat production, while Espinosa-López et al. [24] modeled the temperature of a 46 kW electrolyzer and fitted the model to the experimental data, where the temperature of the stack is also measured. The heat of the stack can also be used, for example, for the preheating the process water, which is analyzed in more detail by Mennilli et al. [25].

Electrolyzer plants can be connected to solar and wind parks to produce green hydrogen. However, the fluctuating operation conditions can damage the MEA of the electrolyzer. A study on a PEM electrolyzer directly linked to a solar cell showed that efficiency decreased after 100 h of variable load conditions. For a more detailed analysis on this subject, refer to [26,27]. The effects of dynamic operating conditions of large scale electrolyzers are analyzed and discussed in detail by Sayed-Ahmed et al. [28]. Even experimental studies are conducted with larger stacks, i.e. [29].

Fitting the model to an electrolyzer requires data on the operating conditions. Brezak et al. [20] reported that gaining knowledge about commercially available electrolyzers is challenging. Indeed, it is particularly challenging if operating conditions can only be derived from the manufacturer's brochures.

In the future, however, newer electrolyzer models may have better efficiency. Makhsoos et al. [30] discuss future perspectives of an increased electrolyzer efficiency due to further research on materials and control strategies.

This paper develops a detailed system model of a PEM electrolysis plant in the megawatt range. Moreover, special attention is paid to analyzing the reaction quotient, the CTC, and the ECD. A PEM stack model is constructed and divided into a time-independent electrochemical submodel using the static approach and a time-dependent thermal submodel using an ODE. The PEM stack model is implemented into the object-oriented Multiphysical Energy System Simulator (MEgy) [31]. MEgy can connect components in the electrical and thermal domains. A network of different components, such as PEM stacks, heat exchangers, and power converters, can be connected to simulate an electrolysis plant of any size.

Among the results of this paper is a critical review of different approaches for setting and/or optimizing the CTC and the ECD values, as reported in the literature. Therefore, these approaches are analyzed, and the differences are presented. In addition, the model is fitted with a sampling optimization to a specific operation point of the Silyzer 300. This optimization process showed that multiple solutions are possible for the ECD for the anode and cathode side, resulting in the same best-fit polarization curve. Based on this, the optimization process showed that the optimization can be achieved by fitting only one parameter. Consequently, fewer parameters need to be fitted, and it can be calculated much faster. Another result is a detailed PEM electrolyzer stack model of the Silyzer 300, which can be used to analyze hydrogen and heat production.

The paper is organized as follows. Section 2 describes the mathematical model and its parameters. Section 3 describes the parameter identification process and introduces, in particular, the new method for optimization of the ECD parameters. Section 4 describes the model validation, and Section 5 discusses results obtained with the current model. Finally, Section 6 summarizes the main findings and gives an outlook on future work.

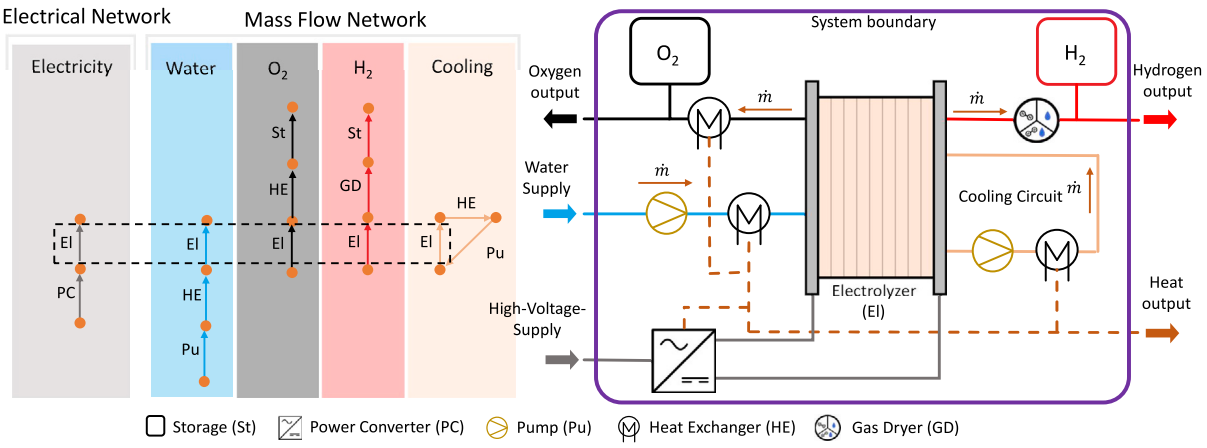

Fig. 1. BoP in MEgy (own work).

2. PEM stack modeling

Modeling a complete megawatt-class PEM electrolyzer power plant involves modeling multiple components. In addition to the PEM stack, other components such as power converters and heat exchangers (the so-called balance of plant, BoP) must be simulated, see Fig. 1. However, in this work, a PEM stack is modeled. The resulting model is implemented in the object-oriented Multiphysical Energy System Simulator (MEgy) [31].

In MEgy, each component, such as a storage tank, compressor, power converter, electrolyzer, or fuel cell, is described in separate classes. The components can be connected in any order and number to form a network via defined interfaces. A single component can be represented in more than one network. An electrical network and a mass flow network are connected. An electrolyzer is present only once in the electrical network but four times in the mass flow network: a subnetwork for each substance (H_2, O_2, H_2O, H_2O-cooling). Modern equations of state such as GERG-2008 are used for the flow network [32]. Thermodynamical data such as heat capacities, enthalpies, and molar masses can be calculated for both pure substances and mixtures. A more detailed description of MEgy can be found in [31].

Additional components are combined into a network to represent an electrolysis power plant in MEgy. Fig. 1 shows a schematic representation of a stack with peripherals. With MEgy, the components can be easily connected in parallel or series, and the entire power plant can be scaled up to several megawatts.

2.1. Thermodynamics

The splitting of water into hydrogen and oxygen is an endergonic reaction. The chemical balance can be split into two half-reactions, one per electrode:

$$\text{Anode:} \quad H_2O \longrightarrow 2H^+ + \frac{1}{2}O_2 + 2e^- \tag{1}$$

$$\text{Cathode:} \quad 2H^+ + 2e^- \longrightarrow H_2 \tag{2}$$

$$\text{Total:} \quad H_2O \longrightarrow H_2 + \frac{1}{2}O_2 \tag{3}$$

Work must be put into the system for the reaction to take place. In the case of electrolysis or fuel cells, the work can be described in terms of non-volume work. The change expresses this in Gibbs energy G (free enthalpy):

$$w_{e,max} = \Delta G \tag{4}$$

G can be calculated using the following equation:

$$\Delta_r G_m = \Delta_r H_m - T \cdot \Delta_r S_m \quad [\text{kJ/mol}] \tag{5}$$

Table 1
Thermodynamic coefficients for the reaction equation $H_2O \longrightarrow H_2 + \frac{1}{2}O_2$ at 25 °C and 101.3 kPa. Values based on [34].

	ΔH_f^0 (kJ/mol)	ΔG_f^0 (kJ/mol)	S^0 (J/(mol K))
H_2O liquid	−285.83	−237.129	69.91
H_2 gas	0	0	130.684
O_2 gas	0	0	205.138

with H being the enthalpy, T the temperature and S the entropy. In the case of electrolysis, $\Delta_r G$ describes the electrical work required to decompose water. Additional energy is required in the form of heat. The heat is described by $T \cdot \Delta_r S$. The change in enthalpy $\Delta_r H$ describes the total energy required [33]. The Gibbs energy for the water decomposition can now be calculated with the Values from Table 1. Eq. (5) is divided between the products and the reactants and multiplied by the stoichiometric factors [33]:

$$\begin{aligned}\Delta_r G_m^0 &= \sum_{R,P}(\nu_P \Delta_f H_{m,P}^0 - \nu_R \Delta_f H_{m,R}^0) \\ &\quad - T \cdot \sum_{R,P}(\nu_P S_{m,P}^0 - \nu_R S_{m,R}^0) \\ \Delta_r G_m^0 &= 0 - \frac{1}{2} \cdot 0 - (-285.83) \\ &\quad - 298 \cdot (0.130684 + \frac{1}{2} \cdot 0.205138 - 0.06991)\ \text{kJ/mol} \\ \Delta_r G_m^0 &= +237.153\ \text{kJ/mol} \ (\text{for } H_2O \rightarrow H_2 + \frac{1}{2}O_2)\end{aligned} \tag{6}$$

The stoichiometric coefficient is denoted by ν with the subscript R for reactants and P for products. The calculation shows that under standard conditions $\Delta_r G_m^0 = 237.153$ kJ/mol of electrical energy is required for the reaction to occur. In addition, the heat energy required can be determined from the equation $T \cdot \Delta_r S_m^0 = 298 \cdot 0.161843 = 48.229$ kJ/mol and the total energy required, $\Delta_r H_m^0 = 285.83$ kJ/mol.

A relationship between thermodynamic properties and an electrical voltage can be established using the following Eq. (7). U_{rev} is called the reversible voltage [35]:

$$U_{rev} = -\frac{\Delta_r G_m^0}{n \cdot F} \tag{7}$$

with F being the Faraday constant and n the number of free electrons in the reaction ($n = 2$). The reversible voltage U_{rev} would occur if two electrodes were immersed in a water-based electrolyte and no current was applied. The negative value indicates that energy needs to be added to the system. If a voltage less than U_{rev} is applied to the cell, decomposition of the water will not occur because there is not enough energy [33].

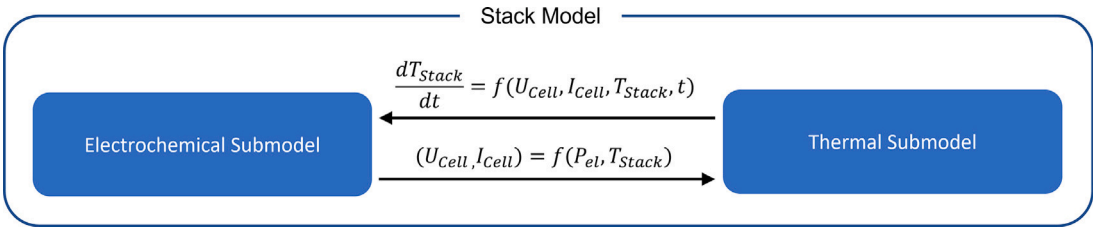

Fig. 2. Correlation between electrochemical and thermal submodel (Based on [24]).

Using the same Equation with the total energy required, $\Delta_r H_m^0 = 285.83\,\mathrm{kJ/mol}$, the thermoneutral voltage U_{tn} can be determined:

$$U_{tn} = -\frac{\Delta_r H_m^0}{n \cdot F} \tag{8}$$

At the thermoneutral voltage U_{tn}, the cell neither produces nor consumes heat. If a cell is operated with a voltage U between U_{rev} and U_{tn}, the electrolysis process would be possible, but the heat from the environment is needed. Otherwise, the cell would continuously cool down, and at the thermoneutral voltage, the reaction rate would be infinitesimally small [23,33]. Hence, the activation energy and the cell resistance must be overcome. Therefore, the cell voltage U_{cell} is always higher than the thermoneutral voltage. Both voltage values are essential characteristics of an electrolyzer because the thermoneutral voltage depends on the chemical substances and the cell voltage in the construction of the cell. The difference $U_{cell} - U_{tn}$ is converted into heat. The heat generated should be removed from the stack to be used for other processes. It follows that the materials and design of a cell are critical to its hydrogen production efficiency. The overall efficiency of a plant can be further increased by using the waste heat.

2.2. Model of the PEM stack

The PEM stack model consists of an electrochemical and a thermal submodel. The electrochemical submodel calculates the polarization curve, which describes the dependence between the current and the voltage. The polarization curve can be calculated in a simplified manner independent of time and location. The thermal submodel determines the stack temperature by balancing the heat gains against the heat losses. This calculation is time-dependent. The correlation between the two submodels is shown in Fig. 2.

2.2.1. Electrochemical submodel

The electrochemical submodel calculates the dependence between a single cell's current and voltage. The cell voltage U_{cell} is composed of the open circuit voltage U_{ocv}, the activation overvoltage U_{act}, the ohmic overvoltage U_{ohm} and the diffusion overvoltage U_{dif}.

$$U_{cell} = U_{ocv} + U_{act} + U_{ohm} + U_{dif} \tag{9}$$

The cell voltage can be linearly scaled, so for the stack voltage and current, it reads:

$$U_{stack} = U_{cell} \cdot n_{cell} \tag{10}$$

$$I_{stack} = I_{cell} = i \cdot A_{me} \tag{11}$$

Open circuit voltage. The open circuit voltage U_{ocv} is described by the Nernst Eq. (12). The first term is the reversible voltage U_{rev} (Eq. (7)). The second term indicates the deviation from standard operating conditions [10,35]

$$U_{ocv} = U_{rev} - \frac{R \cdot T_{stack}}{n \cdot F} \cdot ln\, q \tag{12}$$

with R being the universal gas constant, T_{stack} the average stack temperature, F the Faraday constant, n the stoichiometric coefficient of the electrons in the half-reactions ($n = 2$) and q the reaction quotient. The reversible Voltage U_{rev} can be calculated with Eq. (7). If the operating condition changes, $\Delta_r G$ also changes. An approximation of the reversible voltage is used to account for the changes. Oliver et al. list different approximations [10]. For this work, the following approximation is used to reduce computational complexity:

$$U_{rev} = 1.229 - 8.5 \cdot 10^{-4} \cdot \left(T_{stack} - 298\,\mathrm{K}\right) \tag{13}$$

The reaction quotient q can be calculated in several ways, as shown in the Results section.

Activation overvoltage. In a chemical reaction, the activation energy must be overcome before the reactants can be converted to products. In electrolysis, a half-reaction takes place at the anode and cathode sides. Both halves contribute to the total activation energy, which is determined by the activation overvoltage.

The temperature, the catalyst material, the wear, and the load influence the required activation energy. Many factors go into the calculation for an accurate determination. However, some factors are difficult to determine and cannot be measured directly. The Butler–Volmer equation can be used to determine the overvoltage in relation to the current density:

$$i = i_0 \left[\exp^{\left((1-\alpha)\cdot \frac{n\cdot F}{R\cdot T}\cdot U_{act}\right)} - \exp^{\left(-\alpha\cdot \frac{n\cdot F}{R\cdot T}\cdot U_{act}\right)}\right] \tag{14}$$

The equation has two terms. For each electrode, one term can be neglected as it becomes small. This allows the equation to be rearranged and applied to the anode and cathode, respectively:

$$U_{act,an} = \frac{R \cdot T}{\alpha_{an} \cdot n \cdot F} \cdot \ln\left(\frac{i}{i_{0,an}}\right) \tag{15}$$

$$U_{act,cat} = -\frac{R \cdot T}{\alpha_{cat} \cdot n \cdot F} \cdot \ln\left(\frac{i}{i_{0,cat}}\right) \tag{16}$$

$$U_{act} = U_{act,an} - U_{act,cat} \tag{17}$$

with $\alpha_{an,cat}$ being the charge transfer coefficients (CTC) and $i_{0,an,cat}$ the exchange current densities. By inserting Eqs. (15) and (16) into Eq. (17), the following equation is obtained

$$U_{act} = \frac{R \cdot T}{n \cdot F} \cdot \left(\frac{\ln(i)}{\alpha_{an}} + \frac{\ln(i)}{\alpha_{cat}} - \frac{\ln(i_{0,an})}{\alpha_{an}} - \frac{\ln(i_{0,cat})}{\alpha_{cat}}\right) \tag{18}$$

The CTC α must satisfy the condition $\alpha_{an} + \alpha_{cat} = 1$. It describes the anode and cathode sides' influence on the overall reaction [35]. The exchange current density i_0 measures the chemical activity at the anode and cathode when the cell is in chemical equilibrium. Essentially, the higher the exchange current density, the lower the energy required to initiate the reaction. i_0 is determined by many physical parameters of the catalyst that are difficult to quantify. Moreover, the material, the dimension, and the properties of the electrodes have an influence. In the literature, the exchange current density and the charge transfer coefficient are used to fit the model to the experimental data.

Ohmic overvoltage. The ohmic overvoltage U_{ohm} combines two effects: the electrical and the ionic losses. The electrical losses can be divided between the current collector and the bipolar plate. Ionic losses occur only at the membrane due to ion transfer within the membrane. Since the electrical losses are much smaller than the ionic ones, they are often neglected [9,24]. In addition, other resistance effects occur due to

improper contact between individual components of a cell and multiple cells. In this work, the electrical and the ionic losses are considered.

$$U_{ohm} = \left(R_{el} + R_{me}\right) \cdot I = \left(R_{cc} + R_{bp} + R_{me}\right) \cdot I \tag{19}$$

$$R_* = \frac{\delta_*}{A_* \cdot \sigma_*} \tag{20}$$

with R_* denoting resistances for the current collector (cc), the bipolar plate (bp), and the membrane (me), δ_* the thickness, A_* the Area and σ_* the conductivity, respectively.

Ionic resistance is caused by the movement of ions through the membrane. The membrane must have poor electrical but good ionic conductivity. To accurately determine the conductivity of the PEM, an empirical method is employed. This approach, originally developed by Springer et al. [36] for a polymer fuel cell, remains the most predominate method used in electrolysis methods.

$$\sigma_m = (0.005139 \cdot \lambda - 0.00326) \cdot \exp\left[1268 \cdot \left(\frac{1}{303} - \frac{1}{T_{stack}}\right)\right] \tag{21}$$

with λ being the water content of the membrane.

Since water is always present at the membrane, the water content can be calculated as follows [23]:

$$\lambda = 0.043 + 17.81 \cdot a - 39.85 \cdot a^2 + 36 \cdot a^3 \tag{22}$$

The activity a for water in the liquid state is 1. By inserting this value into Eq. (22), it follows that λ is $\approx$ 14. However, Abdin et al. have described the water content as being between 12 and 14 when the membrane is in 100% water vapor. For liquid water, the value is approximately 22 [11]. Carmo et al. highlight inconsistencies in the literature regarding water content; however, they do not provide a specific reference range [9].

Ohmic losses occur mainly in the current collector and the bipolar plate with further electric losses occurring between individual components due to being incorrectly aligned or unevenly manufactured. These effects however, are not taken into account. Electrical losses vary due to the different material properties and geometry. Materials with good conductivity cause low losses. The bipolar plate has channels for the process and cooling water. Some studies create an equivalent electrical circuit diagram to consider the geometry, i.e., in [9,11,13]. This work calculates the electrical resistance with Eq. (20).

Diffusion overvoltage. Diffusion overvoltage considers the limitation of mass transport from the substances to the electrodes. The membrane electrode assembly (MEA) is entirely surrounded by water during normal operation, which means that the gases produced must be transported away from the MEA in the form of gas bubbles. For this purpose, the gas bubbles travel through the current collector to the bipolar plate, and from there, they are led out of the electrolyzer cell. At high current densities, however, it can happen that the gas bubbles cannot be transported away fast enough. Thus, the water is kept away from the membrane, and the electrolysis process is hindered. This phenomenon can no longer be observed in commercial models [9,15,17]. During operation, the current density must not surpass the manufacturer's specified limit, which is influenced by the design, materials used, and operating conditions. In this study, we model a commercial electrolyzer and consequently neglect the diffusion overvoltage.

2.2.2. Mass flow

The production of hydrogen and oxygen can be assumed to be proportional to the current. Often, the actual amount of hydrogen produced can be adjusted by the Faraday efficiency. However, in line with other researchers, this study assumes the Faraday efficiency is set to $\eta_F = 1$ [17,24] Another factor to consider is that hydrogen is not produced immediately when the current is increased. For this reason, García-Valverde et al. [15] introduced a first-order delay in modeling hydrogen production. Although not considered in this study, it could be a valuable addition to the model. Olivier et al. [10] report that a PEM stack responds relatively quickly to current changes after about 50 ms. The mass transport can be calculated with:

$$\begin{aligned} \dot{n}_{H_2O} &= \frac{I}{2 \cdot F} \cdot \eta_F & \dot{m}_{H_2O} &= \frac{I}{2 \cdot F} \cdot \eta_F \cdot M_{H_2O} \\ \dot{n}_{H_2} &= \frac{I}{2 \cdot F} \cdot \eta_F & \dot{m}_{H_2} &= \frac{I}{2 \cdot F} \cdot \eta_F \cdot M_{H_2} \\ \dot{n}_{O_2} &= \frac{I}{4 \cdot F} \cdot \eta_F & \dot{m}_{O_2} &= \frac{I}{4 \cdot F} \cdot \eta_F \cdot M_{O_2} \end{aligned} \tag{23}$$

with η_F being the Faraday efficiency, $\dot{n}_*$ the molar flows, $\dot{m}_*$ the mass flows, and M_* the molar Mass for the respective substance.

2.2.3. Thermal submodel

The thermal submodel calculates the stack temperature, which determines the cell voltage. In PEM electrolysis, electrical energy is injected into the system to split water. The excess energy is transferred to the stack in the form of heat, which causes the stack to heat up. In order to prevent the stack from overheating and to maintain an optimum operating temperature, the heat must be dissipated by cooling in a controlled manner. For the heat dissipation of the stack, a widely used model is the first law of thermodynamics for open systems. Here, it reads:

$$\frac{dE}{dt} = \dot{W}_{el} - \dot{Q}_{loss} - \dot{Q}_{cooling} + \sum_{out} \dot{m}_{out} h_{out} - \sum_{in} \dot{m}_{in} h_{in} \tag{24}$$

with E being the total inner energy, t the time, $\dot{W}_{el}$ electrical work, $\dot{Q}_{loss}$ heat losses to the environment, $\dot{Q}_{cooling}$ cooling heat, $\dot{m}_*$ mass flows and h_* specific enthalpies. The index *in* denotes inputs, *out* outputs.

Lumped thermal capacity model. The lumped thermal capacitance model is a simple form of transient thermal conduction. This approach assumes a homogeneous temperature throughout the stack [10,15,23,24,37]:

$$\frac{dE}{dt} = C_p \cdot \frac{dT}{dt} \tag{25}$$

The heat capacity C_p describes how fast the stack changes its temperature. Since the stack is considered a single unit with a homogeneous temperature in this model, a unique thermal capacity must be defined. However, the PEM stack consists of several components made of different materials. Therefore, a uniform heat capacity is determined as follows [23]:

$$C_{p,stack} = \sum c_{p,i} \cdot V_i \cdot \rho_i \tag{26}$$

with $c_{p,i}$ being the specific heat capacity, V_i the volume and ρ_i the density of the respective material.

Electrical work. The electrical work converts a portion of its energy into heat, which can be calculated with the thermoneutral voltage U_{tn} (Eq. (8)). This function is based on [15,23,24], but it is extended with the Faraday efficiency because a small portion of the input power is lost due to diffusion losses [38].

$$\dot{W}_{el} = n_{cell} \cdot (U_{cell} - U_{tn}) \cdot I_{stack} \cdot \eta_F \tag{27}$$

Heat losses. The lumped thermal capacity model is applied again. It is assumed that the stack is a body with a homogeneous temperature. The heat transport to and from this body takes place via conduction, radiation, and convection. Not all phenomena can be represented exactly in a model, so simplifications are assumed. The losses will be calculated as follows [37,39]:

$$\dot{Q}_{loss} = h_c \cdot A_o \cdot \left(T_{stack} - T_{atm}\right) = \Phi \cdot \left(T_{stack} - T_{atm}\right) \tag{28}$$

with h_c being the heat transfer coefficient, A_o being the stack's area, $\Phi = h_c \cdot A_o$ being used for the parameter identification process, and T being the stack's and the atmosphere's temperature, respectively. In some models from the literature, the heat transfer coefficient is considered constant. In other cases, it is assumed to be proportional to the current [10].

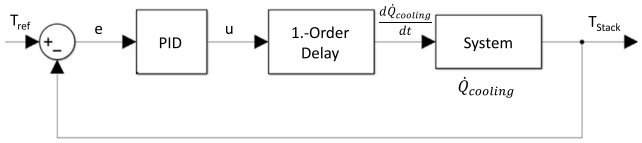

Fig. 3. Block diagram of the cooling circuit (own work).

Transfer between the system and its surroundings. In the case of PEM electrolysis, process water enters the system, which is then split up, and oxygen and hydrogen are expelled from the system. To guarantee sufficient water availability at the membrane, an excess of process water is circulated through the stack. This surplus water exits the stack and undergoes some temperature change. For simplicity, it is assumed, that no heat is extracted through the process water. So, these inflow and outflow terms mathematically negate each other due to the absence of temperature variation. For other substances, the heat can be calculated as follows:

$$\begin{aligned}\sum \dot{m}_{out} h_{out} - \sum \dot{m}_{in} h_{in} = {} & \dot{m}_{O_2,out} \cdot h_{O_2,out}(T_{stack}, p_{an}) \\ & + \dot{m}_{H_2,out} \cdot h_{H_2,out}(T_{stack}, p_{cat}) \\ & - \dot{m}_{H_2O,in} \cdot h_{H_2O,in}(T_{preHeatedWater}, p_{an})\end{aligned} \tag{29}$$

Cooling circuit. For PEM electrolysis of water, energy must be added to the system. In total, more energy is injected than needed for the splitting process. Excess energy is released to the stack in the form of heat, which causes the stack to heat up. To prevent the stack from becoming too hot and to maintain an optimum operating temperature, the heat must be dissipated in a controlled manner by cooling the stack. $\frac{dE}{dt} = 0$ is the target, and ideally:

$$\dot{Q}_{cooling} = \dot{W}_{el} - \dot{Q}_{loss} + \sum \dot{m}_{out} h_{out} - \sum \dot{m}_{in} h_{in} \tag{30}$$

Due to the delay of the cooling system, a temperature change is still possible. Therefore, a PID controller is implemented to keep the temperature constant and controlled to a set point.

A first-order delay element is implemented to simulate the cooling circuit's delay. It represents the delay of the cooling effect, such as the start-up of pumps and valves. A linear time-invariant delay element of the first-order is chosen with parameters K_{PT1} and τ_{PT1}:

$$\frac{d\dot{Q}_{cooling}}{dt} = \frac{K_{PT1} \cdot u - \dot{Q}_{cooling}}{\tau_{PT1}} \tag{31}$$

A first-order delay element has a decisive disadvantage in practice. The behavior of the element is determined by the time constant τ_{PT1}, which specifies how long it takes until 63% of the input variable is reached [40]. This constant is valid for any input. If the input is doubled, the first-order delay element will reach twice the output value after the same time τ_{PT1}.

A proportional–integral–derivative (PID) controller is used to maintain a reference temperature T_{ref}:

$$e = T_{ref} - T_{stack} \tag{32}$$

$$u = K_p \cdot e + K_i \cdot \int_0^t e(\tau)\, d\tau + K_d \cdot \frac{de(t)}{dt} \tag{33}$$

with K_p, K_i, and K_d being the amplification factors of the PID controller. The total control diagram is shown in Fig. 3. The temperature is the controlled value. T_{ref} should be set to the operating temperature of the stack. The parameters K_p, K_i, and K_d for the PID controller should be adjusted to keep the stack temperature below 100 °C in all operating conditions.

2.2.4. Efficiency

Efficiency is defined as the ratio of output to input. When considering a PEM electrolysis plant, several efficiencies can be defined:

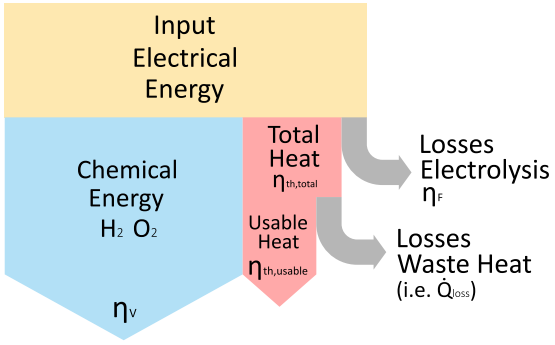

Fig. 4. The input power is mainly distributed between the chemical energy and the heat output. The losses from electrolysis and waste heat cannot be utilized. The diagram is based on [38], but the system boundary in this paper is reduced to the boundary of a stack (own work).

the voltage efficiency, the Faraday efficiency, the stack efficiency, the system efficiency, the total thermal efficiency, and the usable thermal efficiency. A schematic distribution of the electrical input power is shown in Fig. 4. This Sankey diagram is based on [38], but Sterner et al. set the losses from the total heat to be due to pipes transporting water and pumps circulating it. In this work, the system boundary is reduced to the boundary of a stack. Therefore, only losses from the stack, for example, $\dot{Q}_{loss}$ are considered.

The voltage efficiency η_V is the ratio of the thermoneutral voltage to the cell voltage. The thermoneutral voltage depends on water's chemical properties and hardly changes in the temperature range from 0 °C to 100 °C [41].

$$\eta_V = \frac{U_{tn}}{U_{cell}} \tag{34}$$

The Faraday efficiency η_F represents the ratio of the real and the theoretical (ideal) production quantity. It considers the hydrogen diffusion losses because the produced hydrogen diffuses through the PEM membrane to the oxygen side, reducing the actual hydrogen quantity at the output. The Faraday efficiency approaches 100% with increasing current density. Therefore, it is sometimes overlooked in the literature for PEM electrolyzers. In this study, diffusion losses were not calculated, so the Faraday efficiency is defined as $\eta_F = 1$ [41].

$$\eta_F = \frac{\dot{n}_{reH_2}}{\dot{n}_{idH_2}} \tag{35}$$

with $\dot{n}_{reH_2}$ the real molar flow rate and $\dot{n}_{idH_2}$ the ideal molar flow rate.

The stack efficiency η_S describes the ratio between the energy input and the hydrogen produced for a stack. If the Faraday efficiency is 1, the stack efficiency equals the voltage efficiency [41].

$$\eta_S = \eta_V \cdot \eta_F \tag{36}$$

The system efficiency depends on the stack efficiency and the efficiency of the BoP.

The total thermal efficiency describes the heat generation based on the power input. In comparison, the usable thermal efficiency describes the useful heat that can be extracted from the stack for further usage.

$$\eta_{th,total} = \frac{\dot{W}_{el}}{P_{el,stack}} = \frac{U_{cell} - U_{tn}}{U_{cell}} \cdot \eta_F = 1 - \eta_S \tag{37}$$

$$\eta_{th,usable} = \frac{\dot{Q}_{cooling}}{P_{el,stack}} \tag{38}$$

3. Parameter identification process

Drawing from an industry example as detailed below, the methodology for determining all the essential parameters for the simulation

Table 2
Overview of the estimated component dimensions and materials.

Part	Dimensions in mm (length × height × width[a])	Number per stack	Material	Ref.
Bipolar plate	1600 × 450 × 12	26	Titanium	Assumption
Current collector	1600 × 450 × 2	50	Sintered titanium powder	Assumption
MEA	1500 × 400 × 0.178	25	Nafion-117	Assumption
End plate	1700 × 500 × 50	2	Stainless steel	Assumption

[a] $width$ is equal to δ.

model is outlined. The process begins with the acquisition of fundamental stack parameters, as discussed in Section 3.2. Afterwards, the processes for calculating parameters for the electrochemical and thermal submodel are described in Sections 3.3 and 3.4, respectively. In particular, a novel optimization approach is introduced in Section 3.3.2.

3.1. Industrial example

Due to its size and industrial use, the Siemens Silyzer 300 is considered, and the parameters of the overall simulation model are adapted to it wherever feasible. Several parameters are needed, which have not been disclosed by Siemens. Therefore, information about the Silyzer 300 is derived from a data sheet [42] or from published talks, e.g. [43–45]. Additionally, missing information is supplemented with parameters from the literature.

3.2. Basic stack parameters

The process of parameter identification mainly relies on data for a stack. However, information about the internal structure and other parameters are unknown. Therefore, images of the Silyzer 300 [43,46,47] are analyzed to estimate the dimensions and characteristics of the plant. Based on this, six stacks are connected in series, and four series are connected in parallel. The dimensions of each stack can also be estimated. From this, the typical thicknesses of a separator plate and a current collector, the number of cells per stack is estimated to be 25. The size of the membrane is estimated to be $A_{me} = 6000\,\mathrm{cm}^2$.

The Silyzer 300 is rated at a power of 17.5 MW. This power is divided between the 24 stacks and the BoP. An exact distribution of the total power among the individual components is unknown. The power consumption per stack can be calculated. Based on [42,44], a specific operating point for a single cell is determined. At 60 °C, it produces 330 kg/h of hydrogen, and has an efficiency of 76.5%. However, for the temperature, it is unclear which output medium [44] refers to. It is also unclear, if the Silyzer 300 has an efficiency of 76.5% at the hydrogen production rate of 330 kg/h. However, it is assumed that this is the operating point at nominal power. Based on this, the current density and the power consumption of a stack can be calculated. By rearranging and modifying Eq. (23) the current density is calculated:

$$i = \frac{\dot{m} \cdot 2 \cdot F}{\eta_F \cdot M_{\mathrm{H}_2} \cdot A_{me}} = 2.4374\,\mathrm{A/cm}^2 \tag{39}$$

With the current density the power consumption of a stack can be calculated with Eqs. (11) and (36):

$$\begin{aligned} P_{el,stack} &= \frac{U_{tn}(60\,^\circ\mathrm{C}, 101\,325\,\mathrm{Pa}) \cdot n_{cell} \cdot i \cdot A_{me}}{\eta_S} \\ &= 701\,349.9\,\mathrm{W} \approx 701\,350\,\mathrm{W} \end{aligned} \tag{40}$$

So a single stack consumes 701 350 W. The ratio of the BoP to the electrolyzer stacks is $\frac{701\,350 \cdot 24\,\mathrm{W}}{17\,500\,000\,\mathrm{W}} \approx 0.962$. Thus, 3.8% of the 17.5 MW is used by the BoP. The values obtained are listed in Tables 2 and 3.

3.3. Parameters for the electrochemical submodel

This section is divided into two parts. The first part analyzes the parameters which are used in the literature. The second part describes the fitting process for the electrochemical submodel in this work.

Table 3
An overview of the parameters for the Silyzer 300.

Properties	Symbol	Value	Ref.
Power (input)	P_{el}	17.5 MW	[43]
Nominal power per stack	$P_{el,stack}$	701 350 W	Calculated
Stacks		24	[43]
Usage of BoP		3.8%	Calculated
Number of cells	n_{cell}	25	Estimated
Stack efficiency	η_S	76.5%	[44]
Active area of the MEA	A_{me}	6000 cm^2	Estimated
Pressure anode		101 325 Pa	[44]
Pressure cathode		101 325 Pa	[44]

3.3.1. Parameter analyses for the electrochemical submodel

Parameters for the open circuit voltage. The reaction quotient q is calculated in the literature using different equations. According to [35], the reaction quotient describes the activity of the products divided by the activity of the reactants:

$$q = \frac{\text{activities of products}}{\text{activities of reactants}} = \prod_J a_J^{\nu_J} \tag{41}$$

where α is the activity, ν is the stoichiometric coefficient, and J is the substance. For pure solids and liquids, an activity of 1 is used because it does not contribute to q [35]. Since the activity of the substances is difficult to calculate, a simplification is made. For ideal gases, the activity can be approximated with [35]:

$$a = \frac{p_J}{p_J^*} \tag{42}$$

where p^* is the vapor pressure of the pure substance J, and p is the vapor pressure of J when it is part of a solution. The approximation of Eq. (42) is particularly severe for electrolyte solutions, where activity coefficients deviate from 1 even for dilute solutions [35]. However, many papers use this approximation. These equations can be found in the literature:

$$q = \frac{\frac{p_{\mathrm{H}_2}}{p^*_{\mathrm{H}_2}} \cdot \sqrt{\frac{p_{\mathrm{O}_2}}{p^*_{\mathrm{O}_2}}}}{a_{\mathrm{H}_2\mathrm{O}}} \qquad [17,35] \tag{43}$$

$$q = \frac{p_{\mathrm{H}_2} \cdot \sqrt{p_{\mathrm{O}_2}}}{a_{\mathrm{H}_2\mathrm{O}}} \qquad [10,11,23] \tag{44}$$

$$q = \frac{p_{\mathrm{H}_2} \cdot \sqrt{p_{\mathrm{O}_2}}}{p_{\mathrm{H}_2\mathrm{O}}} \qquad [8,9,12,13,24,48] \tag{45}$$

$$q = 1 \qquad [15] \tag{46}$$

Inserting Eq. (42) into Eq. (41) leads to Eq. (43). Based on the citation number, this equation is rarely used. The Eq. (44) can be created by setting $p_J^* = 1$, which can be done if the cell is in the equilibrium state. In Eq. (45), the pressure of the water is used in the divider instead of the activity of the water. The Eq. (46) results in the second term of the Nernst equation (Eq. (12)) being neglected.

As most papers do not calculate the partial pressure, Eq. (45) is usually used. The total pressure at the anode and cathode side is used for p_{H_2} and p_{O_2}. Espinosa-López et al. [24] calculate the partial pressure by using the saturation vapor pressure of water and subtracting it from the

total pressure at the anode and cathode sides, respectively. Espinosa-López et al. use Eq. (45); Therefore, it is assumed that Espinosa-López et al. use the partial pressure for p_{H_2} and p_{O_2}. Keller et al. [17] use Eq. (43) and they calculate the partial pressure using the moisture of the hydrogen and oxygen, respectively. However, Keller et al. do not describe a formula to go from the molar moisture flux of a substance to the partial pressure.

These examples show inconsistency in the literature in calculating the reaction quotient. Therefore, the reaction quotient in this work is simplified to $q = 1$. Besides Eq. (45), setting the output pressure of 1 bar for both the anode and cathode sides of Silyzer 300 also results in a reaction quotient of $q = 1$. This eliminates the second term of the Nernst equation (Eq. (12)). García-Valverde et al. [15] do the same by neglecting the second term of the Nernst equation.

Parameters for the activation overvoltage. Mainly, there are two factors to identify, the charge transfer coefficient (CTC) α and the exchange current density (ECD) i_0, respectively, for the anode and cathode. These values are usually used to fit the model to the experimental data. This section will highlight the inconsistency found in the literature regarding these values. The fitting process for the ECD of this work is shown in Section 3.3.2.

Charge transfer coefficient. The CTC value should satisfy $\alpha_{an}+\alpha_{cat} = 1$. Atkins et al. [35] describe that $\alpha = 0.5$ can be assumed for most chemical reactions. This is also a common argument for solving the Butler–Volmer equation on the basis of symmetry [11]. Furthermore, based on [9,11,13] $\alpha_{an} = 2$ and $\alpha_{cat} = 0.5$ are commonly used. However, these values violate the valid range for the CTC values. Abdin et al. [11] point out that this is due to a faulty analysis model.

Fig. 5 shows the CTC values of different papers. For the cathode side, the value 0.5 is mainly used (Fig. 5(b)). On the anode side (Fig. 5(a)), a wider range of values is used. The fitting process determines some of these. For example, Biaku et al. [12] fitted the α_{an} by setting $\alpha_{an} = 0.5$. The values for the cathode side are the same for most papers, probably due to the small influence on the polarization curve. More attention is paid to the CTC values for the anode side. In Biaku et al. [12] (ID 6), Abdin et al. [11] (ID 7) and Keller et al. [17] (ID 12) a temperature dependence of the anode value is considered. All these studies demonstrate that this value increases with rising temperature.

Exchange Current Density. The ECD i_0 describes the chemical activity at the anode and cathode when the cell is in chemical equilibrium. As the cell's temperature increases, the ECD increases as well. In the literature, many different values exist for this factor. Fig. 5c and d shows several papers' ECD for the anode and cathode sides. The curves with ID 2,4,5,6,7,11,14 are temperature dependent, and the other curves use a static value for the entire temperature range. Due to the large range of values on the anode side, the y-axis is on a logarithmic scale.

García-Valverde et al. [15] (ID 4 and 5) make the ECD temperature dependent by applying the Arrhenius expression. They neglect the ECD on the cathode side because it is a small proportion of the total activation overvoltage. The Arrhenius expression is, therefore, only applied to the anode side, which should lead to an increase in the temperature range of the simulation model. However, it does not represent the actual ECD.

Marangio et al. [13] (ID 8 and 10) calculate the parameters for the ECD at the cathode side by fitting the model to experimental values. In their paper, most of the activation overvoltage is on the cathode side. For this reason, only the ECD of the cathode side is analyzed. The value assumed for the anode side is not specified in their work.

In most cases, the ECD increases with rising temperatures except for the curve for the anode side from Biaku et al. [12] (ID 6). This curve decreases as the temperature rises.

Fig. 5c and d shows a significant difference in the ECD values, especially for the anode side. The difference on the anode side is in the range of 10^9 between the lowest and the highest value.

Table 4
Reference list for Fig. 5.

ID	References	Comments
1	[11]	
2	[19]	
3	[15]	The CTC values are used for UPCT and AIST
4	[15]	For UPCT, the curve is for $i_{0,cat}$, due to the range it is plotted in the anode plot
5	[15]	For AIST, the curve is for $i_{0,cat}$, due to the range it is plotted in the anode plot
6	[12]	Only averages are used
7	[49]	No temperature range is given for α. It is assumed to be identical with the ECD
8	[13]	@20 bar
9	[13]	@70 bar
10	[13]	
11	[24]	Only $\alpha = 0.024$ V is printed It is calculated with $\alpha = \frac{R \cdot T}{2 \cdot 0.024\,\mathrm{V} \cdot F}$ No distinguish between anode and cathode is made
12	[17]	
13	[9]	
14	[23]	
15	This work	

The ECD significantly affects the polarization curve, shown in Fig. 6. The fitted polarization curve of this work is also plotted as well. The other four curves are generated by changing only the ECD on the anode or cathode side, respectively. The lowest and highest values from Fig. 5c and d were used to show the sensitivity of the ECD on the polarization curve.

The sensitivity of the ECD value for the anode and cathode sides on the polarization curve is identical. However, the range from the literature is more significant for the anode side. This results in a more distinction on the polarization curve when using the values for the anode side, as illustrated in Fig. 6.

Several papers show significant inconsistencies for the ECD and CTC values. Additionally, different papers use different equations for the overvoltages. For instance, Olivier et al. [10] list six different equations for the activation overvoltage alone, resulting in different parameters being employed. Importantly, the significant difference of the ECD for the anode side indicates that this value is a fitting parameter without any physical relationship to a cell's actual material or dimensions. Likewise, this is also true for ECD and CTC values for the anode and cathode side, respectively. A physical relation of these parameters would be beneficial to understand the models in more detail. However, these values cannot be measured, but theoretically, the same cells should have nearly identical values. Standardizing the equations for the overvoltages would lead to a better comparability of the values. Thus, models and the corresponding physical cell with the same properties can be understood in more detail and compared. Nevertheless, standardizing the equations does not imply that these values are physically related.

So far, the ECD and CTC values from the literature cannot be used to fit a model with nearly the same properties (materials, dimensions) because these values do not represent any physical relation to a cell, and all the other fitting parameters for the overvoltages also need to be known. Furthermore, the impact on the polarization curve is significant, making it inappropriate to select a value arbitrarily or based on similar cell properties. Thus, the model must always be fitted to the physical measurement data of a cell or stack.

Due to these inconsistencies, the model's values are obtained by numerically fitting the polarization curve to a specific operation point. This process is described in a later section.

Parameters for the ohmic overvoltage. The parameters for the ohmic overvoltage mainly depend on the thickness and material of the stack components. An analysis of the component thickness and the materials used for the Silyzer 300 is described at the beginning of Section 3.

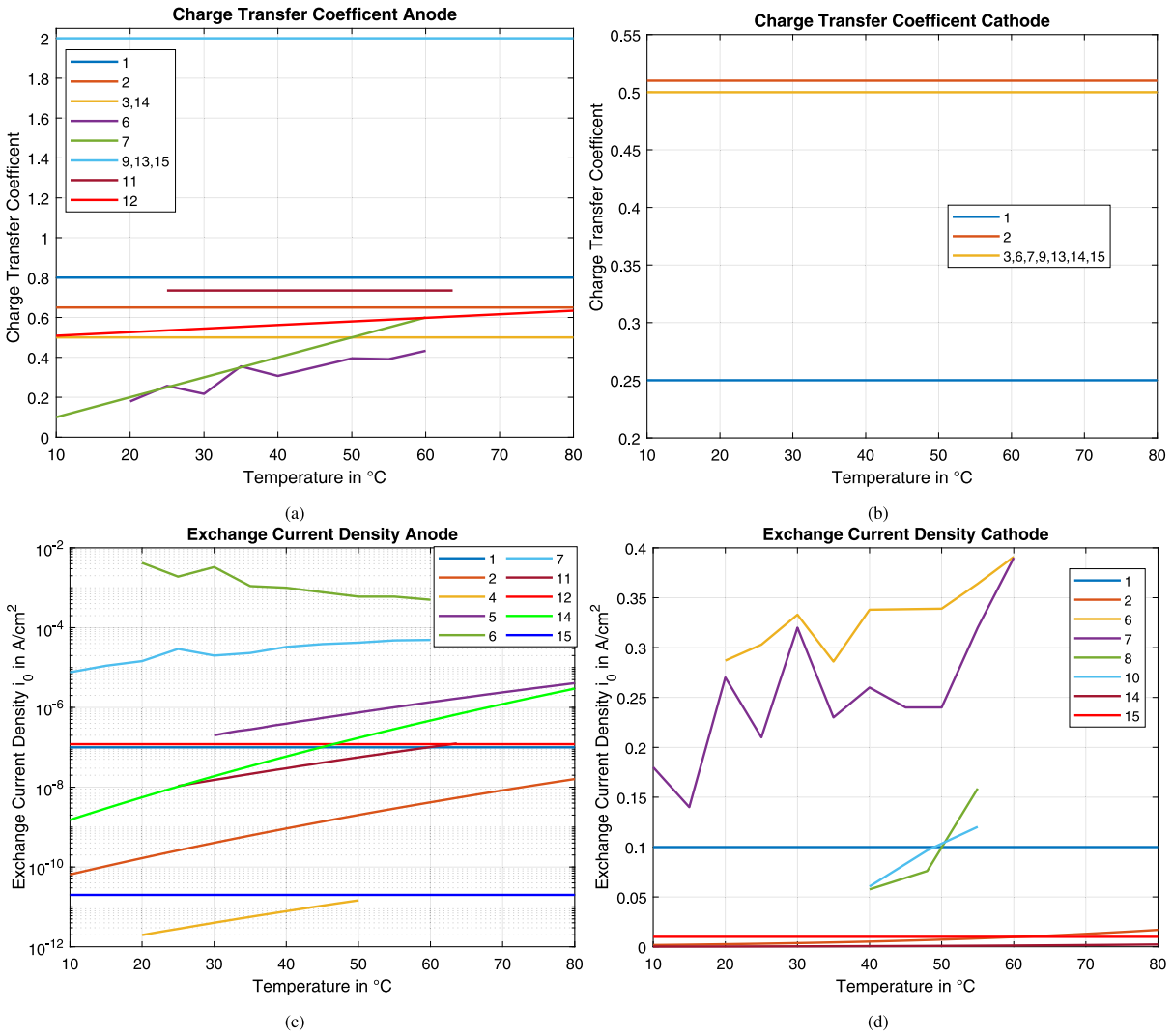

Fig. 5. Overview of the CTC values for the anode (a) and cathode (b) and for the ECD for (c) the anode and (d) the cathode from different papers. A Reference list is in Table 4 (own work). (For interpretation of the references to color in this figure legend, the reader is referred to the web version of this article.)

A list of the parameters is in the Table 6. Only the conductivity of the membrane is calculated with an empirical expression (Eq. (21)). According to Tiktak, the water content can be calculated with Eq. (21) and with $\alpha = 1$ it follows that λ is 14 [23]. However, Abdin et al. [11] describe that λ for liquid water is about 22 and for 100 °C hot water vapor λ is between 12 and 14. In PEM electrolysis, liquid water is present at the membrane. Thus, according to Abdin et al. a λ of 22 would have to be used. Table 6 lists the parameters that are used.

3.3.2. Parameter fitting for the electrochemical submodel

Using experimental data or the datasheet is necessary to fit the model to the Silyzer 300. In Section 3, a stack's power consumption and current density are calculated assuming that it operates at 60 °C with an efficiency of 76.5% and produces 330 kg/h hydrogen. This assumption helps to determine the voltage operation point, which is used to fit the model.

$$U_{fp} = \frac{P_{el,stack}}{I_{stack}} = \frac{P_{el,stack}}{i_{stack} \cdot A_{me} \cdot n_{cell}} \approx 1.9183\,\text{V} \tag{47}$$

Based on the calculation, the cell operates at 1.9183 V and 2.4374 A/cm^2. This point is used to fit the model.

In Section 3.3.1, the parameters for calculating the cell voltage U_{cell} are analyzed and compared to those used in the literature. Certain parameters can be easily determined and estimated by guessing the material and dimensions. However, other parameters cannot be determined or estimated, so they can be used as fitting parameters, primarily ECD and CTC.

The CTC can be set by applying the expression $\alpha_{an} + \alpha_{cat} = 1$ and sticking to $\alpha_{an} = 0.5$ and $\alpha_{cat} = 0.5$ based on [35]. As a consequence, the ECD for the anode and cathode side are the only fitting parameters left in order to fit U_{cell} to U_{fp}.

An error value is calculated to fit the ECD by subtracting the cell voltage from the cell operation point.

$$U_{er} = \left| U_{fp} - U_{cell}(60\,^\circ\text{C}, 2.4374\,\text{A/cm}^2, i_{0,an}, i_{0,cat}) \right| \tag{48}$$

Two methods for fitting the ECD values are used and compared in the this study. Method 1 uses an experimental design of parameter sets to find many equally appropriate approximate solutions of an optimization problem, rather than one only, as typically performed. Method 1 is applied to the ECD parameters here, but could also be used also for optimizations with CTC and ECD values. Method 2 shows that in our case the commonly addressed issue can mathematically be reformulated into a one-parametric optimization problem for an auxiliary variable that is used afterwards to set up a function relating the two ECD values. Note that both methods (brute-force search and auxiliary variables) can easily be combined to allow for (pre)optimization of CTC

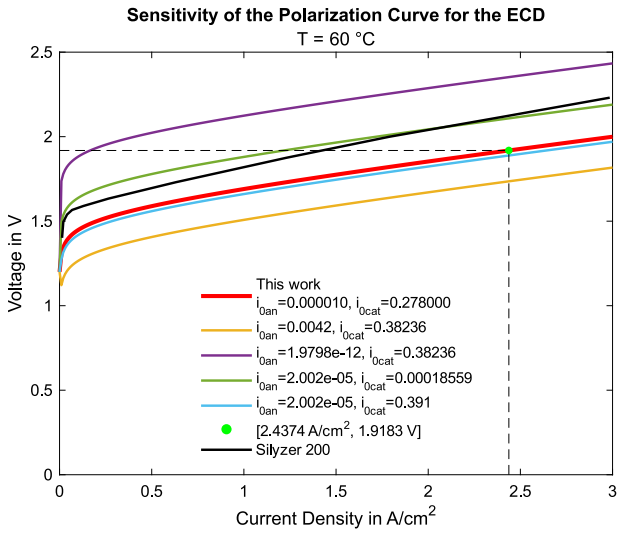

Fig. 6. The sensitivity of ECD. The data for the Silyzer 200 is taken from [50] (own work). (For interpretation of the references to color in this figure legend, the reader is referred to the web version of this article.)

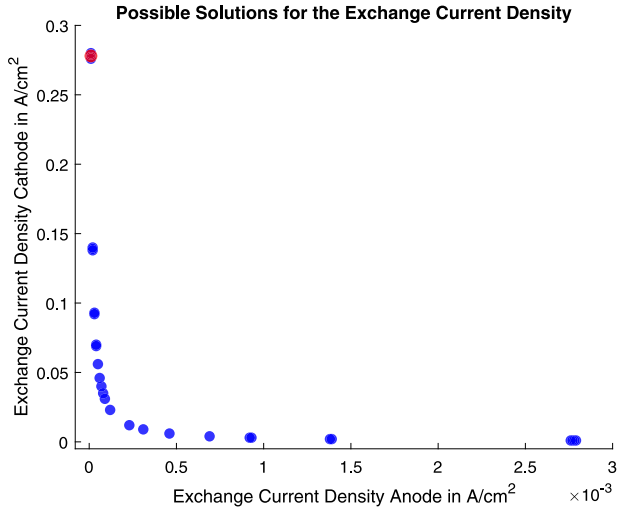

Fig. 7. 30 ECD combinations with the lowest error values (own work). (For interpretation of the references to color in this figure legend, the reader is referred to the web version of this article.)

and ECD values simultaneously. To increase accuracy, the parameter sets found can be used as initial values for local optimization runs.

Method 1 — Naive brute-force search for two parameters. The error is calculated by iterating over ECD values. The ECD values range from 10^{-12} to 10^{-2} with an accuracy of 10^{-5} on the anode side and from 0 to 0.4 with an accuracy of 10^{-3} on the cathode side. These ranges are taken from the literature analysis in Fig. 5c and d. As a result of this iteration, a matrix is obtained which stores the ECD combinations and the respective error values U_{er}. By sorting this matrix w.r.t. error values, the lowest values can be obtained. 30 of them give the lowest error values. They are plotted in Fig. 7.

Which ECD combination is the best possible solution is still unknown. Therefore, the effect on the polarization curve at different temperatures for each ECD combination is analyzed. Fig. 8 shows that all 30 ECD combinations give more or less identical polarization curves per temperature. Zooming in on one cluster of polarization curves shows that multiple curves are plotted next to each other. The

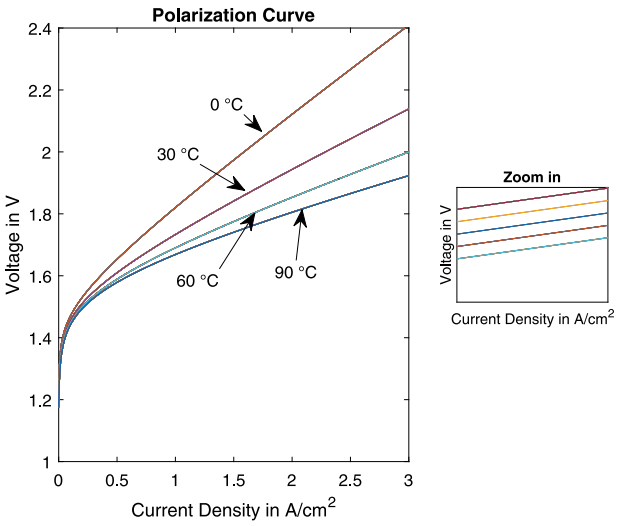

Fig. 8. Polarization curves with all 30 ECD combinations at four different temperatures (own work).

highest difference between the 30 different polarization curves for one temperature is below 10^{-4}.

Consequently, all 30 ECD combinations can be used as fitting parameters for this model. Even when the temperature changes, no significant difference can be seen. For the sake of simplicity, the value combination with the lowest error U_{er} is taken. This results in $i_{0,an} = 1.0000001 \cdot 10^{-5}$ and $i_{0,cat} = 0.278$, which is also marked in Fig. 7 with the red dot.

Method 2 — Optimization of one auxiliary parameter. Although Method 1 gives numerically valid combinations of the ECD values, it is based on the assumption that two independent parameters are still present. However, according to Eq. (9) and by neglecting the diffusion overvoltage, the following optimization problem has to be solved here:

$$\min \left| U_{fp} - \left(U_{ocv} + U_{act} + U_{ohm}\right)\right| \quad \text{for } i_{0,an} > 0,\ i_{0,cat} > 0 \tag{49}$$

where only U_{act} is dependent on the ECD values. According to Eq. (18) and the fact that the CTC values have been fixed to 0.5 each, U_{act} becomes

$$U_{act} = \frac{R \cdot T}{0.5 \cdot n \cdot F} \cdot \left(2\ln(i) - v_{aux}\right) \tag{50}$$

with $v_{aux} := \ln(i_{0,an}) + \ln(i_{0,cat})$. Hence, Eq. (49) becomes

$$\min \left| U_{fp} - \left(U_{ocv} + U_{act} + U_{ohm}\right)\right| \text{ for } v_{aux} > 0 \tag{51}$$

The numerical solution of this optimization problem gives a (unique) optimal value $v_{aux,opt}$. Based on this, a function relating the ECD values is obtained as result of the overall identification process:

$$i_{0,cat} = \exp\left(v_{aux,opt} - \ln(i_{0,an})\right) \tag{52}$$

De facto, this function is depicted (with 30 points) in Fig. 7. Without more information or assumptions on the chemical processes, all ECD values obtained by this function can be used.

3.4. Parameters for the thermal submodel

Lack of data for the Silyzer 300 makes it difficult to determine the parameters for the thermal submodel. Therefore, the available information in the literature for different stacks is used.

Table 5
Data used to calculate C_p.

Part	Material	Specific heat capacity c_p in J/(kg K)	Total volume V in m^3 based on Table 2	Reduced volume V in m^3	Density ρ in kg/m^3	Ref
Bipolar plate	Titanium	513	0.22464	0.1891	4510	Value at 0 °C [34]
Current collector	Sintered titanium powder	513	0.072	0.0432	4510	Value at 0 °C [34]
End plate	Stainless steel	460	0.0850	0.0765	7900	[34]

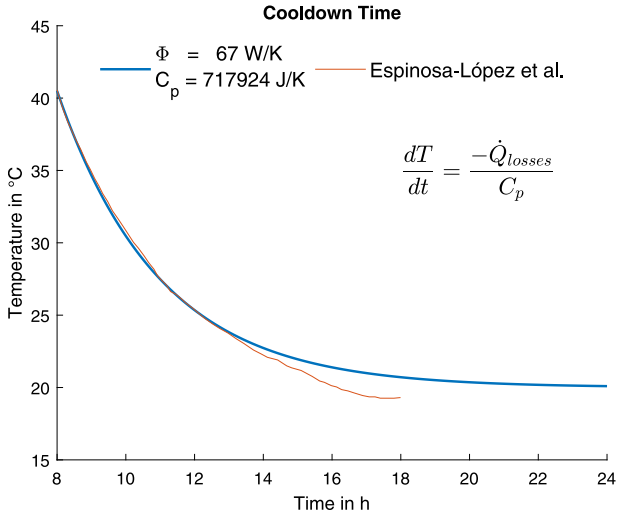

Fig. 9. The 46 kW Giner INC stack is used to fit the model cooldown time (own work).

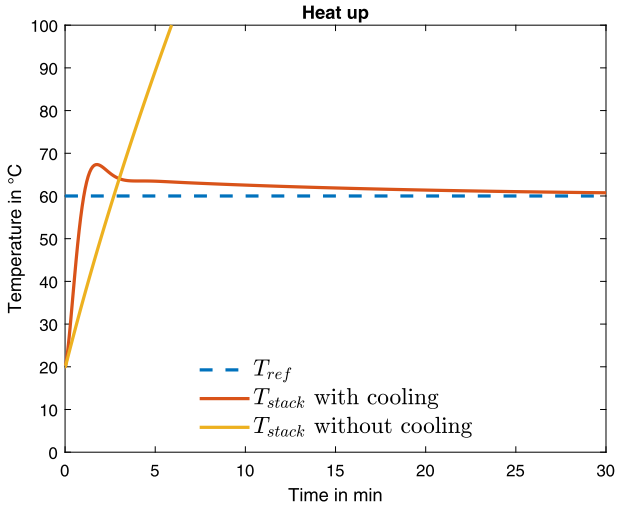

Fig. 10. Comparison of the heat-up time for a stack with and without the controller for the cooling system (own work).

Parameters for the thermal heat capacity and the heat losses. The heat capacity C_p and the heat transfer coefficient h_c greatly influence the stack's cooling behavior.

The heat capacity C_p can be calculated based on estimating the materials and dimensions discussed at the beginning of Section 3. Therefore, taking Eq. (26), the specific heat capacity, the volume, and the density of the materials are necessary.

The materials used for a stack from the Silyzer 300 can only be estimated based on typical materials used in a PEM electrolyzer. Moreover, a comprehensive overview of the materials can be found in Carmo et al. [9]. The specific heat capacity and density values are sourced from existing literature [34]. However, due to insufficient information, the specific heat capacity and density of the sintered titanium powder are equivalent to that of titanium.

An analysis of images from the Silyzer 300 is carried out to estimate the volume of the components. The findings from this analysis are detailed at the start Section 3. The impact of the channels inside the bipolar plate and the porosity of the current collector is considered by reducing the volume. The actual channel design inside the bipolar plate is unknown, so a CAD design with basic channels is created. Based on this, the volume of the bipolar plate is calculated to be 0.005 651 7 m^3 per plate and 0.146 944 2 m^3 per stack. The current collector is porous to ease the transport of liquids and gases between the membrane and the bipolar plate. Grigoriev et al. [8] analyze the overall porosity and pore size distribution. Based on their results, the best porosity could be achieved with 35–40%. So, the volume of the current collector is reduced by 40%. The volume of the end plate is reduced by 10% because it does not have many channels for liquids and gases, and the main task is to stabilize the whole stack. Unfortunately, a detailed analysis of end plates could not be found in literature. The heat capacity is calculated with the values from Table 5 and Eq. (26), resulting in $C_p = 717\,924$ J/K.

The heat transfer coefficient can be calculated with Eq. (28). To ease the fitting process $\Phi = h_c \cdot A_o$ is introduced. In order to determine the appropriate value for Φ, the cooldown time of the current stack model can be compared with that of a similar model or experimental data. In this case, the study conducted by Espinosa-López et al. [24] on the cooling behavior of a 46 kW stack from Giner INC can serve as a reference. However, the main issue with using this data for fitting purposes is that the stack size of the Giner INC model differs significantly from that of the Silyzer 300, which has a much larger stack. However, Fig. 9 shows the cooldown time of the Giner INC stack and the fitted curve. Furthermore, the equations and parameters used are also listed in Fig. 9. Thus, the fitted Φ can be used for the initial model approach. Nevertheless, it must be adjusted later to account for the larger stack used by the Silyzer 300.

Parameters for the cooling circuit and the PID controller. The implemented controller greatly influences the cooling system $\dot{Q}_{cooling}$ and is crucial for simulating with various input powers. It must be ensured that the stack temperature stays below 100 °C, which is not possible without a cooling system for this stack size. In Fig. 10, the heat-up phase of a stack is shown with and without the cooling system. The stack is powered with the nominal power consumption of 700 kW, and the start temperature is 20 °C. It is shown that without the cooling system, the stack reaches 100 °C in less than 6 min. Consequently, a cooling system is required. The controller's parameters must be fitted to ensure the stack temperature stays below 100 °C at varying input powers. In the best case, an oscillating stack temperature should be avoided. The controller's parameters are fitted to satisfy the conditions below 100 °C without oscillation. As it does not affect the model results, for this study, a detailed analysis was not conducted. The fitted parameters are listed in Table 6.

4. Validation of the model

In this section, first there is an analysis of the overall performance of the model, which encompasses a combination of both submodels. Second, a comparison with the actual production values from the model and the Silyzer 300 is presented.

Table 6
An overview of the model parameters used.

Properties	Symbol	Value	Comment
Power (input per stack)	P_{el}	701 350 W	Calculated in Section 3.2
Number of cells	n_{cell}	25	Estimated
Active membrane area	A_{me}	6000 cm^2	Estimated
Pressure anode	p_{an}	101 325 Pa	[44]
Pressure cathode	p_{cat}	101 325 Pa	[44]
Heat capacity	C_p	815 445 J/K	Calculated in Section 3.4
Factor for the $\dot{Q}_{cooling}$	Φ	67 W/K	Calculated in Section 3.4
Atmosphere temperature	T_{atm}	293.15 K	Assumption
Preheated water	$T_{preHeatedWater}$	323.15 K	Assumption
Reference temperature	T_{ref}	333.15 K	Assumption
Thickness bipolar plate	δ_{bp}	12 mm	Estimated
Thickness current collector	δ_{cc}	2 mm	Estimated
Thickness MEA	δ_{me}	178 µm	Estimated
Charge transfer coefficient anode	α_{an}	0.5	Defined
Charge transfer coefficient cathode	α_{cat}	0.5	Defined
ECD anode	$i_{0,an}$	1.000 000 1 × 10^{-5} A/cm^2	Calculated in Section 3.3.2
ECD cathode	$i_{0,cat}$	0.278 A/cm^2	Calculated in Section 3.3.2
Lambda water content	λ	22	Defined in Section 3.3.1
Amplification factor	K_p	50 000	Fitting parameter
Amplification factor	K_i	50	Fitting parameter
Amplification factor	K_d	1 000 000	Fitting parameter
Time constant	τ_{PT1}	50	Fitting parameter
Amplification factor system	K_{PT1}	1	Fitting parameter
Faraday efficiency	η_F	1	Assumption
Reaction quotient	q	1	Discussed in Section 3.3.1
Conductivity bipolar plate	σ_{bp}	133.3 S/cm	[9]
Conductivity current collector	σ_{cc}	145 S/cm	[23]

4.1. Validation of the dynamic behavior of the model

The model is validated with a power input curve, and the output is analyzed. Therefore to achieve this, a power curve is inserted into the model. Based on the data presented in Fig. 11, it can be observed that the reference temperature of 60 °C can be effectively maintained with the given input signal. The signal gradually rises from half the nominal power to full nominal power, followed by a drop in the signal level and a very noisy signal. The temperature curve plotted against this input signal confirms the efficiency of the PID controller in maintaining the reference temperature. Nevertheless, the curve also indicates slight fluctuations in the temperature, with variations of a few degrees being observed.

Challenging scenarios are also observed at 0 min. The stack starts with a stack temperature of 60 °C, and the input power jumps directly to half of the nominal input power. Due to the delay of the cooling system, which is implemented with Eq. (31), the temperature increases rapidly to 61.5 °C and cools down to around 60.5 °C in under 10 min. An input jump to the nominal input power is also possible, and it can be seen in Fig. 11. This result shows that the controller is capable of dealing with high input jumps and quickly keeping the temperature of the stack close to the reference temperature. Nevertheless, a better performance could be achieved during slow ramp-up and ramp-down processes. The temperature rises or falls slowly during the time range of 10–20 min and 30–40 min. In these cases, the controller should be able to adapt quickly and hold the reference temperature. A feed-forward controller such as that developed by Keller et al. [17] can perform better in diverse cases like those presented here.

Additional output results are not shown here because most are proportional to the input curve and do not vary over time. These parameters are time-independent, for example, the hydrogen production rate and cell voltage.

The validation of the model shows that a dynamic behavior can be simulated, even in challenging cases. Nevertheless, there is still room for improvement, especially the controller, which is connected to the cooling system.

4.2. Validation with the Silyzer 300

During the second validation, the model is operated at its nominal power for a duration of one hour. The values for a single stack are scaled up by multiplying it by 24 to reflect the entire electrolyzer plant's capacity. The amount of hydrogen and oxygen produced during this stage is then compared with the data obtained in [44]. The results of this comparison are presented in Table 7. Although the model produces the same amount of hydrogen as the Silyzer 300 plant, the oxygen production rate varies. This variation however, is due to the rounded value from the source [43–45]. According to the stoichiometric equation, the molar ratio should be 2 : 1. However, the molar ratio may vary slightly due to nonideal gas behavior, but this can be neglected here. For the values from [44,45], the ratio is 1.94 : 1. Consequently, the values are rounded, and it is unknown which value is rounded. Regarding other sources, the hydrogen production rate of the Silyzer 300 varies. In [44,45] it is 330 kg/h, but in [43] it is 335 kg/h.

Additional, in Section 3.3.2 the operating point of 1.9183 V and 2.4374 A/cm^2 is calculated. At this point, the model should produce 330 kg/h hydrogen with an efficiency of 76.5%. In Fig. 6, the green dot shows the calculated point. The dashed line marks the actual operation point of the model at nominal power. No significant difference is shown between these points.

Furthermore, the Siemens Silyzer 200 values can be used for validation. In Fig. 6, the polarization curve for the Silyzer 200 is plotted. This curve is taken form [50]. Fig. 6 shows that the polarization curve is slightly higher than the fitted curve of this work. The slope is nearly identical. Since this curve is from the previous model, the Silyzer 200, an improvement in the stack performance is assumed. Thus, the polarization curve from the Silyzer 300 should be lower than the one from the Silyzer 200.

The resulting thermal energy can also be calculated from the model. In this case, the thermal output is also aggregated over the duration of one hour. The usable thermal energy is 161.75 kW/h at a temperature of 60 °C. The problem is that no comparison can be made with the Silyzer 300 because no information about thermal energy output can be found. The output temperature is taken from [44]. However, it is unclear if it is the stack operating temperature or the temperature after the water was reused inside the plant, for example, for pre-heating the process water.

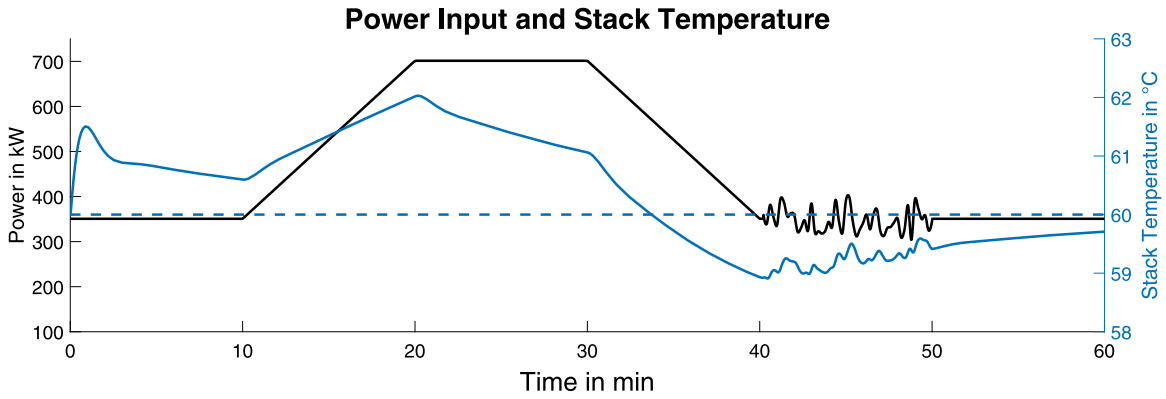

Fig. 11. The input signal in black results in the output stack temperature curve in blue (own work). (For interpretation of the references to color in this figure legend, the reader is referred to the web version of this article.)

Table 7
Comparison of production volume between Silyzer 300 and model.

	Silyzer 300			Model		Difference	
	kg/h	kmol/h	Ref.	kg/h	kmol/h	kg/h	kmol/h
Hydrogen	330	163.70	[44,45]	330.00	163.70	0.00	0.00
Oxygen	2700	84.38	[44,45]	2619.09	81.85	80.91	2.53
Ratio		1.94:1			2:1		
Thermal output per stack				161.75 kW_{th}/h			
Thermal output per plant				3.882 MW_{th}/h			

A comparison can be made between the thermal efficiencies (Eqs. (37) and (38)). The total thermal efficiency $\eta_{th,total}$ is 23.50%, and the usable thermal efficiency $\eta_{th,usable}$ is 23.06%. The difference between the efficiencies is minimal. This means that nearly all the heat produced from the stack can be utilized further. However, this is probably very hard to achieve technically. In addition, according to [44], the Silyzer 300 stacks are air-cooled. When stacks are air-cooled, gaining much thermal energy out of the air is difficult. Therefore, the usable thermal energy calculated by the model is too high and must be readjusted.

The model uses a separate cooling circuit for the cooling water to calculate the heat production, while the Silyzer 300 is air-cooled. Nevertheless, the model can be used to simulate the Silyzer 300, as most of the heat in the Silyzer 300 is dissipated via the process water. In the model, however, no heat is dissipated through the process water; instead, all heat dissipation occurs via the cooling water. The amount of heat within the stack is calculated in the model. How this heat is dissipated is initially irrelevant from a mathematical point of view. Therefore, this model can be used for air-cooled electrolyzers as well.

Consequently, in this study the hydrogen production rate of this model can be adjusted to a specific operation point. However, if the production rate from the actual Silyzer 300 is unclear, the model can just be fitted to the best-known values. Also, more data is required to fit the model more accurately to the Silyzer 300. This need is evidenced by the model's calculated thermal energy output being excessively high when compared to the thermal efficiencies.

5. Discussion

5.1. Discussion about the literature analysis and parameter fitting

This study involved contrasting various equations and parameters cited across multiple studies. Our research revealed discrepancies in the formulas used for the reaction quotient and substantial variation in the values for the Charge Transfer Coefficient (CTC) and the Exchange Current Density (ECD).

This study showed that the calculation of the reaction quotient for the open circuit voltage varies across different studies. As the literature suggests, the reaction quotient is the ratio of activities of the products and the reactants. In order to approximate the activity, the partial pressure-to-pressure ratio is used. However, there are inconsistencies in the literature regarding the calculation of the reaction quotient, and different equations and pressure values used. For instance, some papers use partial pressure, like in [17,24], while others prefer the output pressure at the anode or cathode side, like in [8,9]. As a result of these inconsistencies, the reaction quotient is set to 1 in this paper, which means that the second term of the Nernst equation is not taken into account. This approach is not optimal, as it oversimplifies the calculation of the reaction quotient and may lead to inaccuracies in the final results.

The activation overvoltage has a crucial impact on the polarization curve. The charge transfer coefficient and the exchange current density parameters are the main parameters that affect the activation overvoltage. Understanding them in more detail is beneficial in understanding the impact on the polarization curve. This paper reviews different CTC and ECD values from the literature revealing a broad spectrum of values. Notably, the ECD for the anode side exhibit a variation by a factor of 10^9. This discrepancy is mainly due to these values being used to fit the model to experimental data. Therefore, the fitted values have no physical relation to the properties of the actual cell. It is worth noting that the ECD is influenced by various factors such as material properties, dimensions, wear, and load of the electrodes. Nonetheless, different equations are used for the activation overvoltage in the literature, resulting in a broader range of these parameters and making it harder to compare.

Furthermore, other papers make an optimization process to fit the ECD value for the anode and cathode side according to the experimental data. However, the optimization process in this study, rather than finding one possible solution, aims at exploring multiple possible combinations of ECD values. Since a condition is missing for fixing at least one of the ECD values physico-chemically, a function can be computed which computes one ECD value from the other to set up combinations which lead to the same polarization curve. Both methods introduced and discussed in Section 3.3.2 give de facto the same resulting set of ECD values.

Moreover, fitting both ECD values for the anode and cathode is unnecessary because no further condition exists between these parameters. Therefore, it adds unnecessary computational overhead to an

optimization process. Hence, Method 2 is proposed. As indicated in Section 3.3.2, a combination of Method 1 and 2 can be used to fit CTC and ECD values at the same time. Khajuria et al. [16] use eight parameters for their fitting process. Based on our proposed Method 2, their parameter set could be reduced to four fitting parameters.

5.2. Model validity and limitations

The model has been adapted to the Silyzer 300. However, there are not enough values to model the actual plant accurately. Despite this, the hydrogen production of the model is identical to that of the actual plant. After all, there is varying data about the hydrogen production of the Silyzer 300, which is also strongly influenced by the operating conditions and temperature at which the plant is operated. As exact information is unavailable, only assumptions can be made. Since the electrochemical submodel is fitted to the hydrogen production rate, an uncertainty of this model still exists. The thermal submodel cannot be validated with data from the Silyzer 300 because an output thermal energy could not be found for comparison. For the thermal submodel, most of the parameters are estimated using assumptions from pictures and literature sources. Therefore, a reasonable validation is not possible. It has been shown that the system gives a thermal output for further waste heat usage. However, the difference between the ideal and the usable efficiency showed that the nonusable heat is unrealistically small. Therefore, the calculated thermal output energy is too high and needs to be reevaluated.

Regarding the nonusable heat, the primary influences are the heat losses $\dot{Q}_{loss}$ to the environment and the thermal heat capacity C_p. The heat capacity is calculated based on estimations of the materials and dimensions, which is highly inaccurate. In addition, the Φ for the heat losses is fitted based on a cooldown curve from a 46 kW Giner INC stack and not from a Silyzer 300 stack.

The model fitting process showed that the electrochemical submodel can be adjusted to the hydrogen production rate of the Silyzer 300. However, the methodology for the thermal submodel has to be reevaluated.

Overall, the model was adjusted to the total power consumption and the hydrogen production rate. This results in one operating condition for the electrolyzer plant. This point was used to fit the electrochemical submodel. Moreover, the polarization curve is similar to results from other studies such as [9,11,15,21,48]. Therefore, the polarization curve can be used to model the electrolyzer stack based on openly available data. Although the polarization curve will not match the actual polarization curve of the Silyzer 300, the method shows that the polarization curve can be adjusted to the electrolyzer stack. Moreover, measurement data is needed to decrease the polarization curve error. In addition, the polarization curve from the Silyzer 200 is plotted in Fig. 6. Assuming that a stack improvement is made, the polarization curve must be lower than the polarization curve of the Silyzer 200. Indeed, the fitted polarization curve of our model is slightly lower.

The model should represent an electrolyzer plant in the megawatt range. RWE plans to build a 2 GW electrolyzer plant in Lingen, Germany [4]. The plant will consist of multiple stack arrays with a capacity of a few megawatts each. The model developed in this paper is an initial step and needs further development to represent a full megawatt plant. However, the model can be scaled up to the size of the Lingen plant by simply increasing its scale as a first-order approximation.

6. Conclusion

In this work, an initial version of a megawatt class electrolyzer has been developed. The model has been divided into a time-independent electrochemical and a time-dependent thermal submodel. These models have been coupled to a fully functional simulation model. Furthermore, a cooling control system has been implemented to keep the temperature of the stack to a specific reference temperature.

This simulation model is adapted to the Siemens Silyzer 300 based on freely available data. However, many values are assumed or estimated based on literature references. Based on an assumed operation point, the model can reproduce the hydrogen production rate of the Silyzer 300. However, due to a lack of data, the thermal output cannot be validated with the Silyzer 300. Instead, the total and usable thermal efficiency are used to validate the thermal output. However, the results indicate that the thermal output is too high and needs to be reevaluated.

A critical review of the charge transfer coefficient and the exchange current density as described in literature has been conducted. These values are mainly used as fitting parameters. The literature uses an extensive range of exchange current density values on the anode side, varying by a factor of 10^9. The sensitivity analysis shows that the exchange current density significantly influences the polarization curve.

Moreover, a novel optimization process for the exchange current density has been developed. Leveraging common assumptions in the literature simplifies the mathematical complexity and computation by reformulating the two-parametric optimization problem to an equivalent optimization problem using only one auxiliary parameter. At the same time, it explains the relationship between the ECD values in form of a function. Another benefit is also a faster computational time.

In order to enable better model validation, the model will be adapted to fit the electrolyzer at the Hochschule Bonn-Rhein-Sieg, University of Applied Science. A similar procedure has been carried out with the fuel cell in [31]. Temperature measurements of the laboratory electrolyzer are developed, and the model will be adapted and scaled up to a megawatt electrolyzer model including the BoP.

The next steps involve analyzing the reaction quotient in more detail, and reevaluating the model. Moreover, the novel optimization method will be further analyzed, especially with respect to extensions involving additional parameters and temperature dependencies. Additionally, the next phase entails the simulation of other components, such as power converters and purification stations, to model an entire electrolyzer plant in the megawatt range.

CRediT authorship contribution statement

Malte Pfennig: Conceptualization, Formal analysis, Methodology, Software, Visualization, Writing – original draft, Writing – review & editing. **Barbara Schiffer:** Formal analysis, Software. **Tanja Clees:** Methodology, Supervision, Writing – original draft, Writing – review & editing.

Declaration of competing interest

The authors declare that they have no known competing financial interests or personal relationships that could have appeared to influence the work reported in this paper.

Declaration of Generative AI and AI-assisted technologies in the writing process

During the preparation of this work the author(s) used GrammarlyGo and DeepL Write in order to make the text more readable and identify any gaps. After using this tool/service, the author(s) reviewed and edited the content as needed and take(s) full responsibility for the content of the publication.

Acknowledgments

This work was supported by the German Federal Ministry of Education and Research [Hydrogen Flagship Project TransHyDE_FP1 MechaMod, grant number 03HY201N]. The authors would like to thank the anonymous reviewers for their valuable suggestions.

References

[1] Ansari D, Grinschgl J, Pepe JM. Elektrolyseure für die wasserstoffrevolution. 2022, http://dx.doi.org/10.18449/2022A58.

[2] Shell starts up europe's largest PEM green hydrogen electrolyser. 2021, URL https://www.refhyne.eu/shell-starts-up-europes-largest-pem-green-hydrogen-electrolyser/.

[3] Pilotanlage h_2-elektrolyse lingen | wasserstoff-projekt von RWE. 2023, URL https://www.rwe.com/forschung-und-entwicklung/wasserstoff-projekte/pilotanlage-h2-elektrolyse-lingen/.

[4] RWE arbeitet mit linde an der entwicklung einer 200 megawatt-elektrolyseanlage in lingen. 2021, URL https://www.rwe.com/presse/rwe-generation/2021-12-20-rwe-arbeitet-mit-linde-an-entwicklung-einer-elektrolyseanlage-in-lingen/.

[5] Seyed Alavi SM, Maleki A, Noroozian A, Khaleghi A. Simultaneous optimal site selection and sizing of a grid-independent hybrid wind/hydrogen system using a hybrid optimization method based on ELECTRE: A case study in Iran. Int J Hydrogen Energy 2024;55:970–83. http://dx.doi.org/10.1016/j.ijhydene.2023.11.110.

[6] van der Roest E, Bol R, Fens T, van Wijk A. Utilisation of waste heat from PEM electrolysers – unlocking local optimisation. Int J Hydrogen Energy 2023;48(72):27872–91. http://dx.doi.org/10.1016/j.ijhydene.2023.03.374.

[7] Clees T. Contingency analysis for gas transport networks with hydrogen injection. Math Methods Oper Res 2022;95(3):533–63. http://dx.doi.org/10.1007/s00186-022-00785-x.

[8] Grigoriev SA, Millet P, Volobuev SA, Fateev VN. Optimization of porous current collectors for PEM water electrolysers. Int J Hydrogen Energy 2009;34(11):4968–73. http://dx.doi.org/10.1016/j.ijhydene.2008.11.056.

[9] Carmo M, Fritz DL, Mergel J, Stolten D. A comprehensive review on PEM water electrolysis. Int J Hydrogen Energy 2013;38(12):4901–34. http://dx.doi.org/10.1016/j.ijhydene.2013.01.151.

[10] Olivier P, Bourasseau C, Bouamama PB. Low-temperature electrolysis system modelling: A review. Renew Sustain Energy Rev 2017;78:280–300. http://dx.doi.org/10.1016/j.rser.2017.03.099.

[11] Abdin Z, Webb CJ, Gray E. Modelling and simulation of a proton exchange membrane (PEM) electrolyser cell. Int J Hydrogen Energy 2015;40(39):13243–57. http://dx.doi.org/10.1016/j.ijhydene.2015.07.129.

[12] Biaku C, Dale M, Mann M, Salehfar H, Peters A, Han T. A semiempirical study of the temperature dependence of the anode charge transfer coefficient of a 6kW PEM electrolyzer. Int J Hydrogen Energy 2008;33(16):4247–54. http://dx.doi.org/10.1016/j.ijhydene.2008.06.006.

[13] Marangio F, Santarelli M, Cali M. Theoretical model and experimental analysis of a high pressure PEM water electrolyser for hydrogen production. Int J Hydrogen Energy 2009;34(3):1143–58. http://dx.doi.org/10.1016/j.ijhydene.2008.11.083.

[14] Alizadeh M, Torabi F. Precise PEM fuel cell parameter extraction based on a self-consistent model and SCCSA optimization algorithm. Energy Convers Manage 2021;229:113777. http://dx.doi.org/10.1016/j.enconman.2020.113777.

[15] García-Valverde R, Espinosa N, Urbina A. Simple PEM water electrolyser model and experimental validation. Int J Hydrogen Energy 2012;37(2):1927–38. http://dx.doi.org/10.1016/j.ijhydene.2011.09.027.

[16] Khajuria R, Yelisetti S, Lamba R, Kumar R. Optimal model parameter estimation and performance analysis of PEM electrolyzer using modified honey badger algorithm. Int J Hydrogen Energy 2024;49:238–59. http://dx.doi.org/10.1016/j.ijhydene.2023.07.172.

[17] Keller R, Rauls E, Hehemann M, Müller M, Carmo M. An adaptive model-based feedforward temperature control of a 100 kW PEM electrolyzer. Control Eng Pract 2022;120:104992. http://dx.doi.org/10.1016/j.conengprac.2021.104992.

[18] Tjarks G. PEM-elektrolyse-systeme zur anwendung in power-to-gas anlagen. Schriften des forschungszentrums Jülich: Reihe Energie & Umwelt, vol. Band 366, Jülich: Forschungszentrum Jülich GmbH, Zentralbibliothek; 2017.

[19] Chandesris M, Médeau V, Guillet N, Chelghoum S, Thoby D, Fouda-Onana F. Membrane degradation in PEM water electrolyzer: Numerical modeling and experimental evidence of the influence of temperature and current density. Int J Hydrogen Energy 2015;40(3):1353–66. http://dx.doi.org/10.1016/j.ijhydene.2014.11.111.

[20] Brezak D, Kovač A, Firak M. MATLAB/Simulink simulation of low-pressure PEM electrolyzer stack. Int J Hydrogen Energy 2023;48(16):6158–73. http://dx.doi.org/10.1016/j.ijhydene.2022.03.092.

[21] Bernt M, Gasteiger HA. Influence of ionomer content in IrO 2 /TiO 2 electrodes on PEM water electrolyzer performance. J Electrochem Soc 2016;163(11):F3179–89. http://dx.doi.org/10.1149/2.0231611jes.

[22] Khalid Ratib M, Muttaqi KM, Islam MR, Sutanto D, Agalgaonkar AP. Electrical circuit modeling of proton exchange membrane electrolyzer: The state-of-the-art, current challenges, and recommendations. Int J Hydrogen Energy 2024;49:625–45. http://dx.doi.org/10.1016/j.ijhydene.2023.08.319.

[23] Tiktak J. Heat management of PEM electrolysis: A study on the potential of excess heat from medium- to large-scale PEM electrolysis and the performance analysis of a dedicated cooling system. 2019, URL http://resolver.tudelft.nl/uuid:c046820a-72bc-4f05-b72d-e60a3ecb8c89.

[24] Espinosa-López M, Darras C, Poggi P, Glises R, Baucour P, Rakotondrainibe A, Besse S, Serre-Combe P. Modelling and experimental validation of a 46 kW PEM high pressure water electrolyzer. Renew Energy 2018;119:160–73. http://dx.doi.org/10.1016/j.renene.2017.11.081.

[25] Mennilli F, Jin L, Rossi M, Comodi G. Heat recovery from a proton exchange membrane (PEM) electrolyser to improve its performance. In: SDEWES 2023 conference proceedings. 2023, (0999–2).

[26] Cai X, Lin R, Xu J, Lu Y. Construction and analysis of photovoltaic directly coupled conditions in PEM electrolyzer. Int J Hydrogen Energy 2022;47(10):6494–507. http://dx.doi.org/10.1016/j.ijhydene.2021.12.017.

[27] Wilberforce T, Olabi AG, Imran M, Sayed ET, Abdelkareem MA. System modelling and performance assessment of green hydrogen production by integrating proton exchange membrane electrolyser with wind turbine. Int J Hydrogen Energy 2023;48(32):12089–111. http://dx.doi.org/10.1016/j.ijhydene.2022.12.263.

[28] Sayed-Ahmed H, Toldy Á, Santasalo-Aarnio A. Dynamic operation of proton exchange membrane electrolyzers—Critical review. Renew Sustain Energy Rev 2024;189:113883. http://dx.doi.org/10.1016/j.rser.2023.113883.

[29] Crespi E, Guandalini G, Mastropasqua L, Campanari S, Brouwer J. Experimental and theoretical evaluation of a 60 kW PEM electrolysis system for flexible dynamic operation. Energy Convers Manage 2023;277:116622. http://dx.doi.org/10.1016/j.enconman.2022.116622.

[30] Makhsoos A, Kandidayeni M, Pollet BG, Boulon L. A perspective on increasing the efficiency of proton exchange membrane water electrolyzers– a review. Int J Hydrogen Energy 2023;48(41):15341–70. http://dx.doi.org/10.1016/j.ijhydene.2023.01.048.

[31] Bareev-Rudy M, Meiswinkel S, Pfennig M, Schedler S, Schiffer B, Steinebach G, Clees T. Analysis of PtGtX systems with metal hydride storage based on coupled electrochemical and thermodynamic simulation. In: 18th. conf. sustainable development of energy, water and environment systems. SDEWES, 2023, (0662–1).

[32] Clees T, Baldin A, Klaassen B, Nikitina L, Nikitin I, Spelten P. Efficient method for simulation of long-distance gas transport networks with large amounts of hydrogen injection. Energy Convers Manage 2021;234:113984. http://dx.doi.org/10.1016/j.enconman.2021.113984.

[33] Millet P, Grigoriev S. Water electrolysis technologies. In: Renewable hydrogen technologies. Elsevier; 2013, p. 19–41. http://dx.doi.org/10.1016/B978-0-444-56352-1.00002-7.

[34] VDI-Wärmeatlas. Berlin, Heidelberg: Springer Berlin Heidelberg; 2013, http://dx.doi.org/10.1007/978-3-642-19981-3.

[35] Atkins PW, de Paula J. Atkins' physical chemistry. 9th ed.. Oxford: Oxford University Press; 2010.

[36] Springer TE, Zawodzinski TA, Gottesfeld S. Polymer electrolyte fuel cell model. J Electrochem Soc 1991;138(8):2334–42. http://dx.doi.org/10.1149/1.2085971.

[37] Mills AF. Basic heat and mass transfer. 2nd ed.. Upper Saddler River, NJ: Prentice Hall; 1999.

[38] Sterner M, Stadler I. Handbook of energy storage. Berlin, Heidelberg: Springer Berlin Heidelberg; 2019, http://dx.doi.org/10.1007/978-3-662-55504-0.

[39] Cerbe G, Wilhelms G. Technische thermodynamik: theoretische grundlagen und praktische anwendungen. 19th ed.. München: Hanser; 2021.

[40] Lunze J. Regelungstechnik 1. Berlin, Heidelberg: Springer Berlin Heidelberg; 2010, http://dx.doi.org/10.1007/978-3-642-13808-9.

[41] Lettenmeier P. Efficiency - electrolysis. 2021, URL https://assets.siemens-energy.com/siemens/assets/api/uuid:a33a8c39-b694-4d91-a0b5-4d8c9464e96c/efficiency-white-paper.pdf.

[42] Silyzer 300: The next paradigm of PEM electrolysis. URL https://assets.siemens-energy.com/siemens/assets/api/uuid:a193b68f-7ab4-4536-abe2-c23e01d0b526/datasheet-silyzer300.pdf.

[43] Regelfähigkeit von elektrolyseanlagen: Am beispiel des silyzer 300. 2021, URL https://netztransparenz.tennet.eu/fileadmin/user_upload/The_Electricity_Market/German_Market/Grid_customers/Kundenforum_2021/4_Kundenforum_30_11_21_Vortrag_Regelfaehigkeit_Elektrolyse.pdf.

[44] PEM electrolyser technology: Flexible, efficient and scalable. 2021, URL https://www.energyforum.in/fileadmin/user_upload/india/media_elements/Presentations/20210714_h2_large/Siemens_Energy.pdf.

[45] Brammen P. HydroHub fenne: Erzeugung von wasserstoff mittels elektrolyseur. 2021, URL https://www.tuvsud.com/de-de/-/media/de/industry-service/pdf/event-downloads/is/h2-forum-saarland/04_hydrohub-fenne_philipp-brammen_steag.pdf.

[46] The global energy transition will be based on the hydrogen economy. 2021, URL https://press.siemens-energy.com/global/de/feature/die-globale-energiewende-wird-auf-der-wasserstoffwirtschaft-basieren.

[47] Schnettler A. At the dawn of the hydrogen economy. 2020, URL https://www.powermag.com/at-the-dawn-of-the-hydrogen-economy/. POWER.

[48] Awasthi A, Scott K, Basu S. Dynamic modeling and simulation of a proton exchange membrane electrolyzer for hydrogen production. Int J Hydrogen Energy 2011;36(22):14779–86. http://dx.doi.org/10.1016/j.ijhydene.2011.03.045.

[49] Dale NV, Mann MD, Salehfar H. Semiempirical model based on thermodynamic principles for determining 6kW proton exchange membrane electrolyzer stack characteristics. J Power Sources 2008;185(2):1348–53. http://dx.doi.org/10.1016/j.jpowsour.2008.08.054.

[50] Buttler A, Spliethoff H. Current status of water electrolysis for energy storage, grid balancing and sector coupling via power-to-gas and power-to-liquids: A review. Renew Sustain Energy Rev 2018;82:2440–54. http://dx.doi.org/10.1016/j.rser.2017.09.003.